The Pennsylvania State University

The Graduate School

DESIGN AND CHARACTERIZATION OF MAGNETIC FIELD ACTUATED MULTILAYERED POLYMERS

A Thesis in

Mechanical Engineering

by

Rui Leng

Submitted in Partial Fulfillment

of the Requirements

for the Degree of

Master of Science

May 2022

The thesis of Rui Leng was reviewed and approved by the following:

Zoubeida Ounaies

Professor of Mechanical Engineering

Thesis Advisor

Mary I Frecker

Professor of Mechanical Engineering

Department Head of Mechanical Engineering

Daniel Haworth

Associate Head for Graduate Programs

ABSTRACT

This thesis investigates multi-field actuated smart materials for potential biomedical applications. Magneto-active elastomers (MAEs) consisting of magnetic particles and a two-part elastomer were first designed and tested for their degree of actuation as unimorphs. The study considered two types of magnetic particles, hard and soft. For hard magnetic particles, barium hexaferrite (BHF) microparticles were chosen based on their responsiveness to magnetic field and their hard magnetic properties. The permanent magnetic dipoles of BHF resulting in large remanent magnetization can be polarized by magnetic field into designed directions. For soft magnetic particles, iron oxide microparticles were chosen where application of magnetic field results in induced dipoles. The elastomer matrix for the MAEs was fabricated using a two-part polydimethylsiloxane (PDMS) base and curing agent. BHF-PDMS and iron oxide-PDMS were fabricated using conventional casting method, processed into unimorphs and actuated as proof of concept. A unimorph structure is a layered structure where a substrate material is deformed using an active material and designed for large bending deformation. Bending and folding actuation was elicited with BHF-PDMS thin films as the particle magnetic dipoles were poled in a uniform direction beforehand. The film then reacts to external magnetic field by aligning the dipole directions with the external magnetic field direction. Iron oxide-PDMS was also studied and actuated using external magnetic field. Other actuation configurations designed included gripping and flower blooming motions. Large bending actuation was achieved with both hard and soft MAEs, and the next step was to test for printability. Iron oxide-PDMS was chosen for the printability test and the material compositions was tuned by adjusting base to curing agent ratio and by the addition of thickening agent. The printability study considered parameters such as temperature and number of printed layers, and results showed that printable iron oxide-PDMS

slurries were obtained with 5wt% fumed silica added. The matrix of the magneto-active polymer-based materials was also investigated by comparing PDMS with mechanically stiffer polyvinyl alcohol (PVA) in degree of actuation. In the last step, multi-field actuation was studied using both conventional casting and additive manufacturing (AM) methods. Shape memory polymers (SMPs) were chosen to act as the "active" substrate for their shape fixing and recovery abilities under different temperatures. Unimorph structures were again used to test actuation of MAE-SMP under both magnetic and thermal fields. A gripping configuration was designed and demonstrated using conventionally cast iron oxide-PDMS and SMPs. Printed iron oxide-SMP thin films were actuated to assess the impact of the functional gradient design, showing different degree of actuation with different compositions of materials.

The outcome of this research aims at potential biomedical applications using smart materials to allow non-contact control with large actuations. Additive manufacturing will enable the facile fabrication of actuators using these multiple materials, and would allow more customized devices to be printed for ease of use, while adapting to each patient's unique condition and requirement.

Table of Contents

List of Tables

List of Figures

Acknowledgement

I would first like to thank Dr. Zoubeida Ounaies for being such an amazing advisor and guiding me through the past two years of research study. I appreciate her support and patience with me through the ups and downs, and I would never be able to accomplish what I have without her trust in me. Dr. Ounaies not only inspired me as a role model with her depth of knowledge and extraordinary achievements in the field, but she also showed me a committed and passionate attitude towards both research and life. I am beyond grateful for having her as my advisor and she owns significant credit for this work. I also thank my committee member Dr. Mary I Frecker for her invaluable suggestions and guidance.

I would like to thank Dr. Amira Meddeb and my lab mates - Xiaoyue, Dash, and Amal- for their unconditional support, helping me when I first joined the lab and being such caring and amazing members. I especially thank Dr. Amira Meddeb for all the trainings and instructions in my experiments, Xiaoyue Zhao for obtaining DMA data and Dashiell Papula for conducting SEM and VSM for my samples.

I am grateful to be a part of LEAP HI project with my advisor and to work with Dr. Carolyn Seepersad and Dr. Oliver Uitz from University of Texas at Austin, and Dr. Mary I Frecker and Tan Pan at Penn State. To be able to know and work with such brilliant scholars was an unforgettable experience and has taught me so much. I also thank Dr. Carolyn Seepersad and Dr. Oliver Uitz for characterizing and printing samples and mailing them across half of the states to our lab.

I would like to acknowledge and thank the National Science Foundation CMMI#: 1953259 for funding our project. The findings and conclusions do not necessarily reflect the view of NSF.

Lastly, I thank my family and friends for their endless support and understanding. I would not have been able to keep pushing myself forward without their encouragements.

Chapter 1

Introduction

1.1 Background and motivation

In recent years, smart materials have been the focus of biomedical device innovations such as bone tissue engineering using shape memory polymers [1], wearable assistive system using material's self-tightening properties [2], and shape memory suture tightening in response to temperature [3, 4]. Smart materials respond to external stimuli such as light, heat and electrical and magnetic fields by deforming and adapting their properties. The ability to actuate smart materials without the need for direct contact, such as with light, heat and magnetic fields, is particularly attractive for many applications. It is important and impactful to develop a way to customize medical devices for patients. For example, when orthopedic devices are needed as remedy, incorporating shape memory polymers (SMPs) into implants saves patients from a second surgery by self-adjusted mechanical properties of the materials [5]. The implants can be deformed using an induction device to trigger the one-way shape memory recovery without incision to the body. As the research in this area keeps advancing, additive manufacturing and novel smart materials have the potential to make customizable medical devices a reality. Additive manufacturing (AM) techniques are known for realizing complex geometries in the structure design. Biomedical devices such as a cardiovascular stent can be customized and printed using stereolithography technique with a complex geometry [6]. The structure printed with SMP can be squeezed into a small shape for the ease of surgery, and expand once inserted at the desired location with the help of body heat. More and more customizable designs are being studied to improve the biomedical field.

1.1.1 Magneto-active polymer-based materials

Responsive polymer-based materials are a type of smart material. Polymer-based materials are chosen for this research study owing to their flexibility and lightweight. Responsive polymer-based materials include magneto-active elastomers (MAEs) which respond to external magnetic field, SMPs which change shape and recover with the change in temperature, and photoactive polyurethanes that respond to light [7].

An MAE is a soft elastomer matrix embedded with magnetic particles. The particles can exhibit hard magnetic or soft magnetic behavior. Actuation is achieved through a torque generated from hard magnetic particles alignment, or by attraction due to induced dipoles from soft magnetic particles. For example, Pirmoradi et al. [8] introduced coated iron oxide particles dispersed in an PDMS elastomer matrix to create a magnetic composite membrane that can be actuated by external magnetic field. The MAE was actuated by attracting the induced dipoles inside iron oxide, which is a soft magnet, and achieved tasks such as rolling and other locomotion. Many studies have shown the potential of actuating MAEs using magnetic field with complex designed shapes.

For magnetic particles, hard and soft magnetic particles in MAEs lead to different material responses due to their different properties as shown in Figure 1. Saturation magnetization is the material's maximum magnetic moment, coercivity determines the resistance of a magnetic material to changes in magnetization, and remanent magnetization is the magnetization remaining in the material after an external magnetic field is removed.

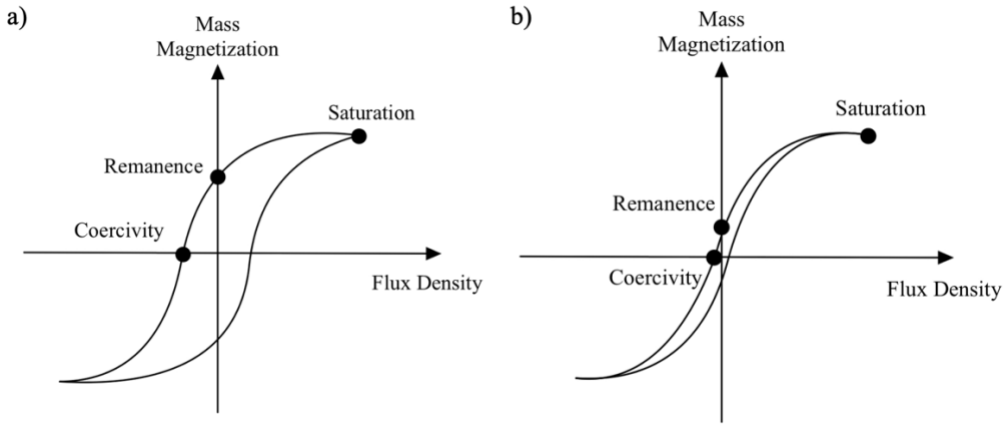

Figure 1. A hysteresis loop showing remanent and saturation magnetizations, and coercivity of magnetic materials. Larger remanent magnetization and coercivity indicates hard magnetic properties (a), while soft magnets obtain little remanent magnetization and coercivity (b).

Hard magnets such as barium ferrite and neodymium iron boron show large coercivities and remanent magnetizations as illustrated in Figure 1, leading to strong magnetic responses [9]. The magnetic dipoles of each particle can be polarized by applying external magnetic field to align with the field directions. After polarizing and fixing the dipole directions into desired patterns, complex actuation responses can be achieved by having the MAE under a uniform magnetic field. For example, Martin et al. [10] demonstrated how using electromagnets to pole the particles created customized patterns inside the matrix for various actuation responses. The particles were first poled in one direction and cured by UV exposure with selective portions, and then poled in a different direction for the uncured portions to create a unique pattern of dipole directions. Barium hexaferrite (BHF) particles particularly have been examined and tested actuation to show the effect of dipole alignments on large degree of actuation. Koo et al. demonstrated actuation using a thin strip of MAE by an electromagnet. The film bent 90° angle

where the dipole directions aligned with the external magnetic field directions as expected [11]. Various complex geometries of possible actuation were investigated by Kim et al. [12], as shown in Figure 2, proving a remote and fast transformation with predesigned dipole directions.

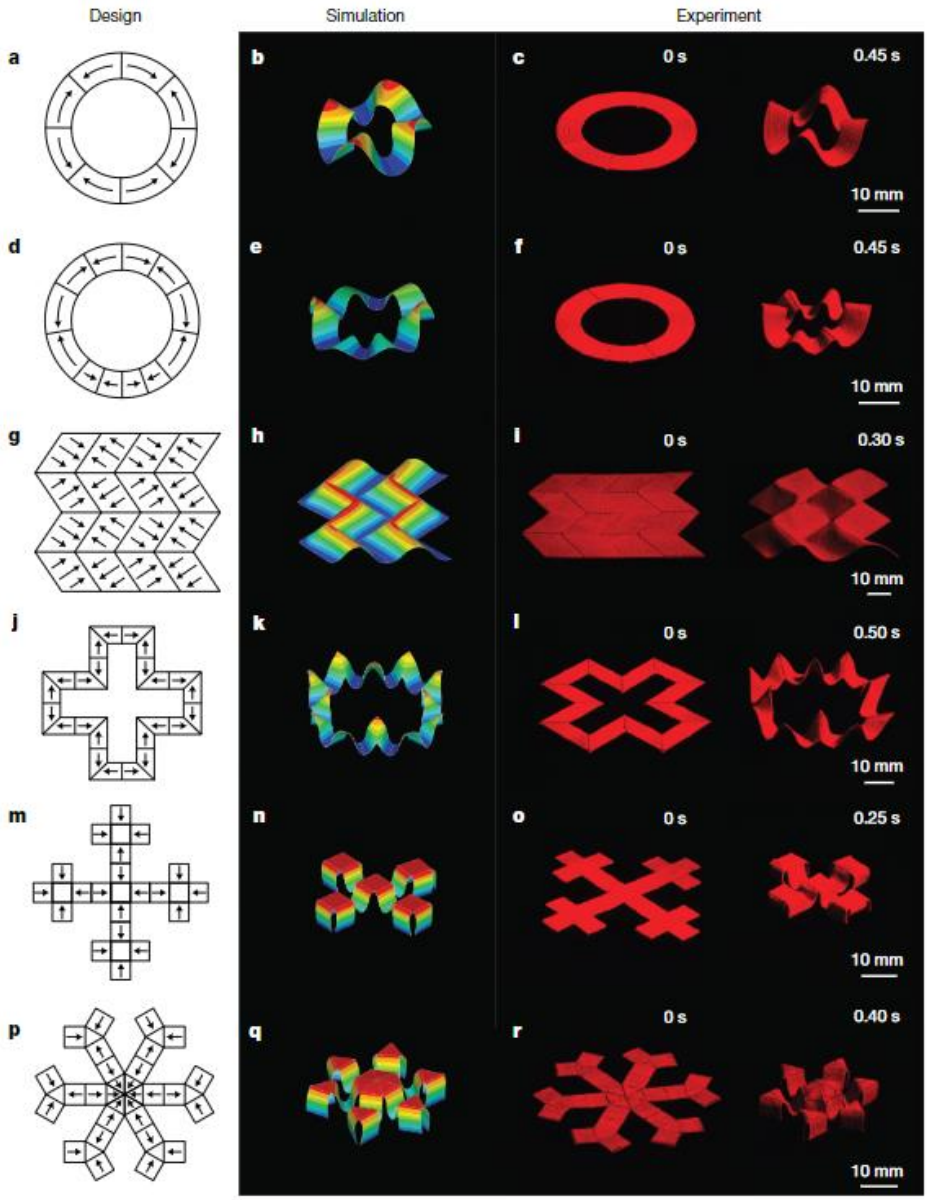

Figure 2. Demonstration of actuation with complex geometries [12].

Soft magnets such as iron oxide and carbonyl iron, on the other hand, have small coercivities and remanent magnetizations and exhibit only induced dipoles when under an external magnetic field [13]. By using a permanent magnet or holding close to one side of the electromagnet, soft MAEs can be actuated without direct contact. For example, Zhu et al. [14] fabricated MAEs into butterfly wings using iron particles and used a moving permanent magnet for actuation of the wings flapping motion, as shown in Figure 3. The wings were attracted by the magnetic field and thus following along the movement of permanent magnet. Fabricating MAEs using iron oxide particles with polydimethylsiloxane (PDMS) into helical coils for rolling actuation was also studied and proved to have remote control over the MAEs [15]. Figure 4 shows untethered locomotion by using a permanent magnet to actuate the helical coil behind a vertical wall, which demonstrates a non-contact actuation.

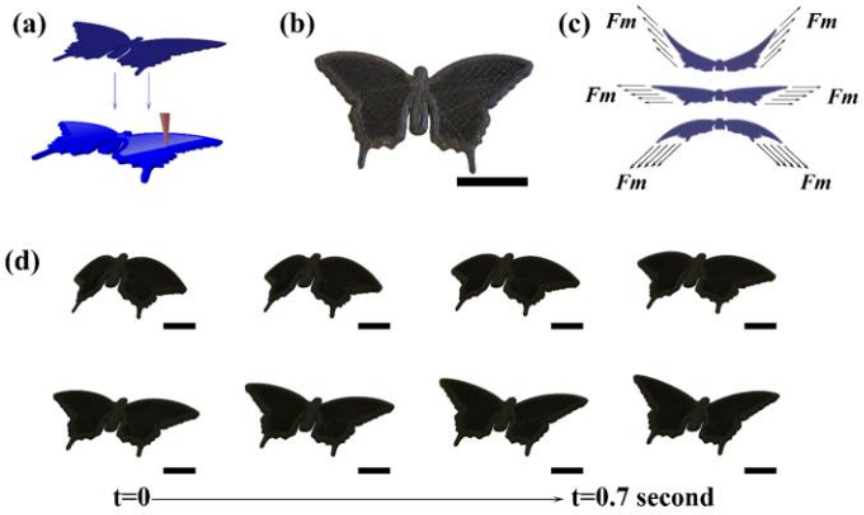

Figure 3. Butterfly wings actuation with (a) a schematic of actuation, (b) an optical image of the butterfly, (c) illustration of the location of magnetic field as butterfly wings flap, and (d) a series of optical images during the flapping of the wings. [14]

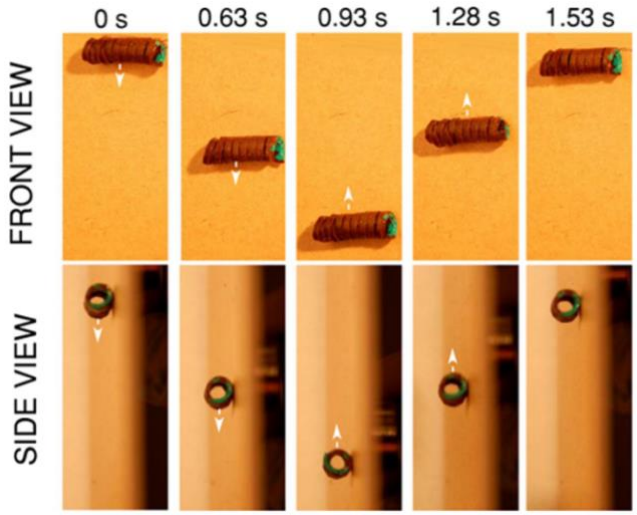

Figure 4. Untethered locomotion of the helical coil on a vertical wall [15].

Hard and soft magnetic particles behave differently when both particles were dispersed in a polymer matrix and result in different magnetic responses. Ze et al. [16] dispersed both neodymium iron boron and iron oxide particles in a shape memory polymer matrix to exploit different magnetic properties of the particles. Hard magnetic particles acted as actuators with polarized dipole directions and soft magnetic particles were used for magnetic inductive heating to soften the SMPs, as shown in Figure 5. The hard magnetic particles were first polarized in designed patterns, and then soft magnetic particles were heated from the heating magnetic field B_h to allow hard magnetic particles to actuation due to the actuation field B_a.

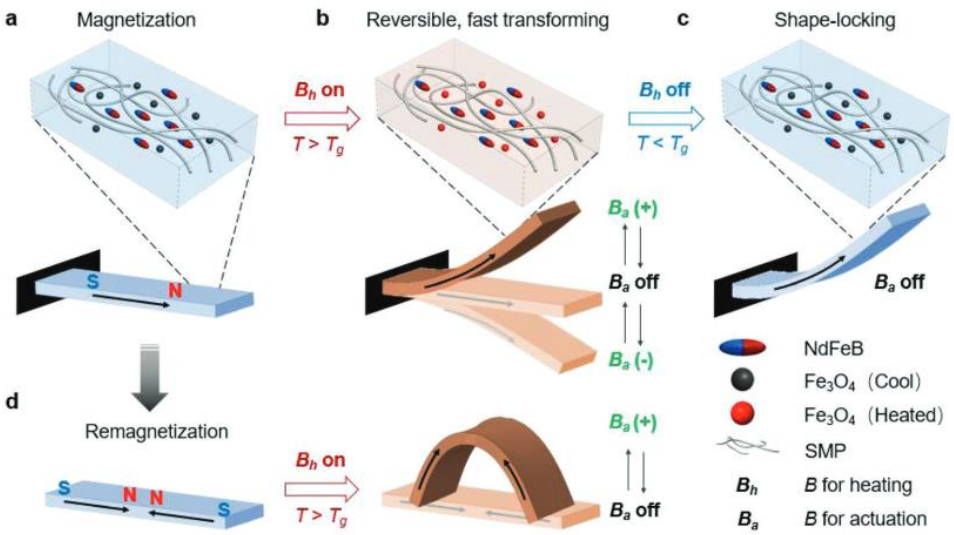

Figure 5. Actuation mechanism of magnetic SMPs [16].

Additionally, macrostructures of MAEs were studied to achieve larger and more complex actuations. Qi. et al [17] incorporated small MAE segments inside a large soft polymer matrix and simulated walking, swimming and gripping motions with the designed structure under external magnetic field. The segments were arranged so that each portion of the matrix reacted to external magnetic field with different directions of local torque generated from MAE segments. Similar research has been conducted by Kimura et al. [18] on varying orientations of short fibers inside polymer matrix to affect the degree of actuation. Cui et al. [19] designed rigid panels carrying single-domain nanomagnets connected by structured hinge springs acting as folding creases as shown in Figure 6. The nanomagnet arrays were magnetized and arranged in two different orientations orthogonal to each other by applying external magnetic field, and the design achieved complex actuation geometries such as showing letters in 16 four-panel units and motions of an origami microscale bird as shown in Figure 7.

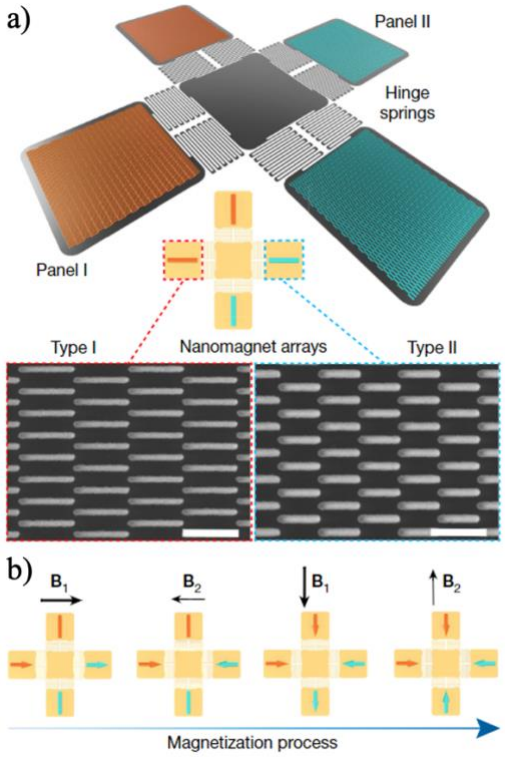

Figure 6. Schematics showing (a) four-panel micromachine with arrays of nanomagnets with corresponding SEM images and (b) encoding of the micromachine using two different fields in different directions [19].

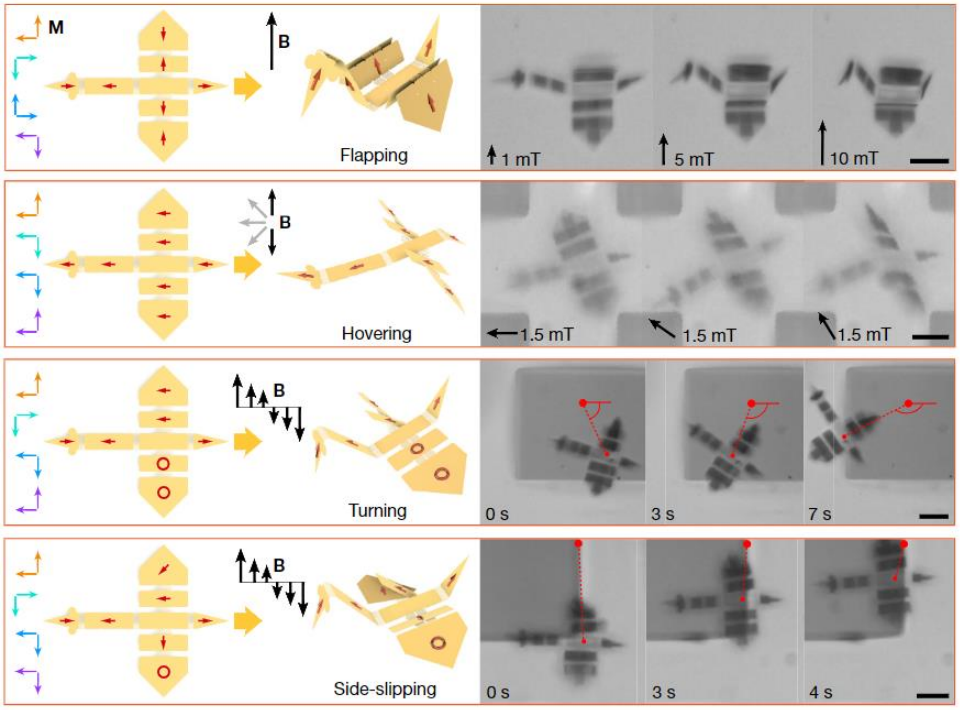

Figure 7. Origami microscale bird with multiple motions [19].

Material choices of polymers used have been investigated as well. Three commonly used matrices are natural rubber, silicone rubber and polyurethane [20]. Natural rubber has great mechanical characteristics and heat resistance for practical engineering applications. Some disadvantages of natural rubber include aging, complex vulcanization process and low reversibility which limit applications and utilization. Silicone rubber, on the other hand, has more simple fabrication processes and adjustable mechanical properties due to curing conditions. Last but not least, polyurethane rubber has high elasticity and resistance and also shape memory effect that allows responsiveness to temperature. Many other matrices studied for magneto-active polymer-based materials include bromobutyl rubber [21] and mixed matrices such as mixed cis-polybutadiene rubber and natural rubber [22]. Based on mechanical properties and

biodegradability, polydimethylsiloxane (PDMS), polyvinyl alcohol (PVA), and epoxy resin are specifically chosen for this study.

Additive manufacturing has played an important role in fabricating magneto-active polymer-based materials. Wu shuai et al. [23] incorporated direct ink writing technique to print NdFeB embedded silicone matrix while polarizing the particle directions around the printing nozzle. The printed polarization pattern changed as the direction of the magnetic field changed, which greatly reduced fabrication time to design complex geometries compared to conventional casting method. Other printing techniques include extrusion [24], fused deposition modeling [25], and fused filament fabrication [15] which are all proved feasible to print magneto-active polymer-based materials.

Two main types of external magnetic field were used to actuate the magneto-active polymer-based materials to obtain different actuation responses. Zhu et al. [14] employed permanent magnets to actuate soft magnetic particles inside MAEs by induced dipoles, where the induced dipoles in the MAEs were attracted by the permanent magnets. Kimura et al. [26] generated magnetic field from an electromagnet connected to a supplied electric current. The arranged hard magnetic particle directions aligned with the external magnetic field and responded based on the anisotropic structure. With the presence of both soft and hard magnetic particles, Ze et al. [16] combined a pair of electromagnetic coils that generate magnetic field for actuation and a solenoid for inductive heating for different types of particles embedded in MAEs.

1.1.2 Shape memory polymers (SMPs)

SMPs are shape-programmable polymers that can be fixed in a temporary position and then recover their permanent shape in response to temperature [3], and prior research has

discussed and analyzed the shape memory effect to a great extent. For example, Tao et al. [27] designed an origami structure using SMPs and studied the deformation by adding loadings on the structure while changing the temperature. The origami structure twisted and compressed at elevated temperature and stiffened at a temporary shape when temperature decreased. SMPs have successfully shown potential in achieving complex geometries with large deformation.

1.1.3 Multi-field stimuli

In order to achieve larger and more complex actuation shapes, combinations of two or more external stimuli have shown great potential. For example, Zhao et al. [28] implemented both light and humidity into control factors and fabricated bio-inspired actuators that deforms under UV light and different humidity levels of the environment. Another example of multi-stimuli actuation is demonstrated by Ze et al. [16] dispersing magnetic particles inside a shape memory polymer matrix so that the composite reacts to both magnetic field and temperature. The abilities of MAEs to deform significantly and SMPs to alter between permanent and temporary positions proved to be a great fit for potential biomedical applications for its non-contact control and thus were selected for this study. MAEs act as the actuator that actively deforms and changes shape, while SMPs act as the substrate to allow bending and folding of the MAEs as well as introduce another external stimulus for more control over the composite. The proposed multi-stimuli design can not only achieve large degree of actuation, but also allow complex actuation geometries.

Additive manufacturing has been a big part of the research field with various materials including polymers, metal, and concrete [29]. 3D printing has shown a great advantage in precise shape control and achieving complex geometries while the conventional casting methods are

more time consuming and difficult to operate. Additive manufacturing allows combination of materials and also the potential to control how and where each material is deposited and layered. For example, Uitz et al. [30] had shape memory polymer printed through *in situ* curing in reactive extrusion and demonstrated printability of additively manufactured shape memory polymers. Bodkhe et al. [31] has combined piezoelectricity with shape memory and carbon fiber by printing shape memory poly-lactic acid with barium titanate through direct ink write. The addition of carbon fiber gave potentials as resistive heating-assisted actuation. 3D printed iron oxide embedded shape memory poly-lactic acid designed by Cheng et al. has been printed into frames and membranes as an atrial septal defect occlude and successfully demonstrated large deformation with magnetic field and heat [3].

1.2 Research objectives and tasks

In order to identify the potential of the multi-field responsive polymer-based composites for biomedical applications, it is important to investigate materials fabrication, characterization, and actuation performance. This thesis aims at developing responsive multi-field polymer-based material systems while using fabrication and characterization to guide the additive manufacturing process. Contactless large deformation of structures with conventionally-cast MAE thin films using both hard magnetic particles BHF and soft magnetic particles iron oxide embedded in a PDSM elastomer matrix were investigated to prove the feasibility of the proposed concept. Additionally, the printability of MAE ink was studied to guide the additive manufacturing, specifically with iron oxide-PDMS composite as a model ink. To better assess the effect of matrix material on the MAE composite actuation, different polymers were selected and compared. Last but not least, MAEs and SMPs were combined through both conventional casting and additive manufacturing for multi-field stimuli actuation using magnetic and thermal fields. To this end, the broad goal of this thesis is to investigate the degree of actuation of the proposed multi-field responsive polymer-based materials and prove the feasibility of replacing conventional casting with additive manufacturing.

To accomplish this goal, the specific objectives and related tasks are:

Objective 1. Proof of actuation and characterization of conventionally-cast MAEs. To accomplish this objective, the following two tasks will be performed:

Task 1.1. Fabricate unimorphs with both types of MAEs (soft and hard) and passive substrate and characterize actuation under magnetic fields for free displacement.

Task 1.2. Design complex geometries such as gripping and flower blooming motions using one or more different compositions of MAEs to prove feasibility of actuation.

Objective 2. Proof of printability of iron oxide-PDMS composite ink. Specifically, this objective is focused on the following two tasks:

Task 2.1. Tune the material composition by adjusting the elastomer base to curing agent ratio and its viscosity by adding fumed silica as thickening agent.

Task 2.2. Investigate the relationship between printing condition, layers printed and printed time for interlayer adhesion.

Objective 3. Effect of matrix materials on the performance of magneto-active polymer-based material. Specifically, this objective is focused on the following two tasks:

Task 3.1. Fabricate PVA and magneto-active materials consisting of PVA and iron oxide microparticles.

Task 3.2. Characterize PVA and iron oxide-PVA and compare with iron oxide-PDMS in degrees of actuation.

Objective 4. Demonstration of multi-stimuli actuation using both magnetic and thermal fields. Specifically, this objective is focused on the following three tasks.

Task 4.1. Fabricate SMPs and demonstrate the shape memory effect with shape locking and recovery processes.

Task 4.2. Design and demonstrate actuation of conventionally-cast MAEs combined with SMPs in gripping actuation.

Task 4.3. Design and demonstrate actuation of additively manufactured MAE-SMP films in thin strip actuation.

1.3 Thesis outline

Chapter 1 discusses the literature with a focus on MAEs and SMPs, their fabrication processes and actuation. The potential of MAEs and SMPs in biomedical applications motivates this research on multi-stimuli responsive polymer-based materials.

Chapter 2 introduces the materials and shares details on the actuation setup and sample dimensions to support result discussions in later chapters. Characterization setups and procedures for both mechanical and magnetic properties of fabricated responsive composites are documented.

In Chapter 3, Objective 1 and 2 of this thesis are addressed. This chapter demonstrates the conventional casting procedures to fabricate MAEs and assess the difference between hard and soft magnetic particles. Poling the particles was introduced by using permanent magnets during the curing process of PDMS elastomer. The fabricated thin films were then compared by measuring the actuation displacement in a unimorph structure. Other actuating geometries such as gripping and flower blooming motions using one or more combined material compositions were demonstrated as proof of concept. Characterizations of the MAEs including tensile tests, optical microscopy (OM), scanning electron microscopy (SEM), vibrating sample magnetometry (VSM) were conducted. In addition, the printability of iron oxide-PDMS composite ink was tested. Material compositions, the addition of thickening agent fumed silica, printing conditions and interlayer adhesions were all investigated.

Chapter 4 addresses Objective 3 of this thesis. In this chapter, the matrix of magneto-active polymer-based materials was studied to assess the effect of different material on the degree of actuation and material responses. 12wt% PVA solutions was fabricated from pure PVA pellets by heating and mixing with distilled water. Hardened pure PVA thin film was

characterized using differential scanning calorimetry (DSC) to analyze the amount of water left in the solution and glass transition temperature (T_g) of PVA. Iron oxide-PVA composites were then fabricated using the prepared 12wt% PVA solutions. Comparison between iron oxide-PVA and iron oxide-PDMS was assessed through actuation displacement measurements.

Chapter 5 discusses Objective 4 of this thesis, namely the SMPs and their shape memory effect. Material chosen was an epoxy resin with a fast-acting curing agent. The shape memory effect was first demonstrated with pure SMP film under thermal control. Combination of conventionally-cast iron oxide-PDMS and SMPs was then actuated in a gripping configuration using both magnetic and thermal fields for proof of concept. Finally, additively manufactured iron oxide-SMP were actuated under both magnetic and thermal fields.

In Chapter 6, significant findings are summarized and research contributions are discussed. The potentials of multi-field responsive polymer-based materials in additive manufacturing are highlighted. Future work of this research is suggested as well.

Chapter 2

Experimental Methods

2.1 Materials

2.1.1 Materials for MAEs

In this study, barium hexaferrite (BHF) and iron oxide microparticles were selected as the magneto-active particles. The BHF microparticles selected were purchased from ESPI Metals, have a size of 1.1 µm wide and 0.15 µm thick, and are identified as hard magnets. Scanning electron microscopy (SEM) was conducted and hexagon-shaped BHF microparticles were observed as shown in Figure 8. It is important to note that the magnetic dipole direction is out of the plane. Iron oxide microparticles were purchased from Atlantic Equipment Engineers, have a diameter of 1-5 µm with 99.9% purity, and are the soft magnets. For this study, the particles were further sieved to reduce the size range and avoid particle agglomerations using a sieve with a mesh size of 180 µm.

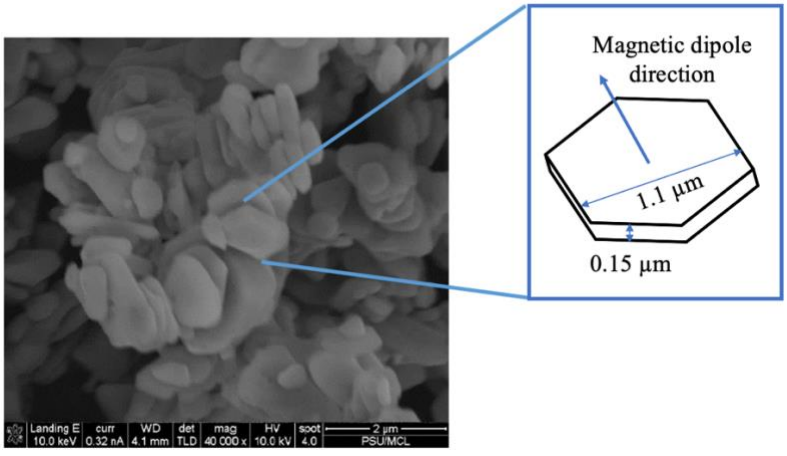

Figure 8. SEM on BHF microparticles [32].

Two polymers were used as the matrix material for the MAEs. Polydimethylsiloxane (PDMS), as shown in Figure 9 for its chemical structure, is a clear two-part silicone elastomer that contains the base and curing agent (Sylgard 184, Dow Corning). It was chosen based on its biocompatibility, lightweight and flexibility. The curing process of PDMS allows the crosslinking between the polymer chains to form and result in an elastomeric polymer that is stretchable. The recommended curing time ranges from 48 hours under 25°C to 35 minutes under 100°C, and the viscosity of base and curing agent mixed is 3500 cP. To dilute the PDMS solution, n-heptane (Acros Organics) was used with 0.0003% residue after evaporation. The solvent has a boiling temperature of 98°C and melting temperature of -91°C.

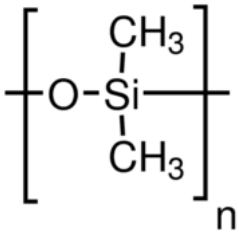

Figure 9. Chemical structure of PDMS.

The second polymer used as the matrix is polyvinyl alcohol (PVA), as shown in Figure 10 for its chemical structure, which is a clear water-soluble polymer. This thermoplastic material can dissolve in water and reform again after water evaporates. The reason that these two materials were selected is because of the difference in stiffness and material properties. Table 1 shows a large difference between the Young's modulus of PDMS and PVA, indicating a much stiffer properties of PVA. The difference in T_g indicates PDMS as thermoset and PVA as thermoplastic.

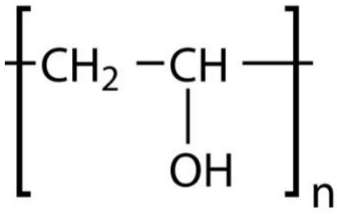

Figure 10. Chemical structure of PVA.

2.1.2 Materials for SMPs

A clear epoxy resin (EPON 8111, Hexion) with a slightly yellow colored hardener (EPIKURE 3271, Hexion) was selected based on its fast hardening, within a minute, which is ideal for AM process for layer adhesion and final product qualities. Once the epoxy and the hardener are mixed together, the exothermic reaction releases heat and the mixture hardens within a minute. Once fully cured, the epoxy cools down and becomes stiff at room temperature. The shape memory process can then be performed by heating above the T_g which is around 50-70°C depending on the process of cure. Once above its T_g, the epoxy becomes soft and can be deformed in to a temporary shape which is then fixed by cooling the epoxy below its T_g. A table comparing mechanical and chemical properties of PDMS, PVA and epoxy resin is shown in Table 1.

Table 1. Properties of PDMS and PVA [30], [33]–[35].

Properties	PDMS	PVA	Epoxy resin
Density (g/cm^3)	1.03	1.31	1.14
Young's modulus (Mpa)	1.32-2.97	707.9	/
Glass transition temperature (°C)	-125	80	50-70
Viscosity (cp)	3500	/	800-1100

2.2 Methods

2.2.1 Fabrication of MAEs

To fabricate the MAEs, mechanical stirrer and bath sonicator were used to mix the particles in the amount of 30 wt% with respect to the polymer matrix solution. The mechanical stirrer chosen was IKA RW 20 digital with a maximum spinning rate of 2000 rpm and the bath sonicator used was from Fisher Scientific with 2.8 L volume. A general flow chart of the fabrication process for MAEs using PDMS is included in Figure 11. The mechanical stirrer mechanically mixed the materials with a stirring blade at around 250 rpm and introduced shear forces to separate the magnetic particles and prevent them from agglomerating. The sonicator created sound waves to vibrate the particles in the water bath and thus help remove any air bubbles trapped inside the solution due to high viscosity. With the combination of mechanical stirrer and bath sonicator, the solution can be uniformly mixed for a high quality and well dispersed solution. After the mixing, the solution was degassed again in vacuum to ensure all air bubbles get eliminated. With PDMS, the curing agent was then added after degassing at a weight ratio of 1:10 curing agent to base. The solutions were cast using a doctor blade, or poured into a petri dish or a premade mold. Out of these three different methods, casting by a doctor blade gives most accurate control of the resulting sample thickness, ranging from 0.05-0.8 mm. The resulting film thickness can be controlled within 0.01 mm difference. Larger variations were usually found in BHF-PDMS films as the magnetic field used to pole BHF affected the positions and directions of the magnetic particles inside the polymer matrix. After casting, solutions were cured in an oven at 100°C for 3 hours or at room temperature for 48 hours. Both methods yielded similar mechanical and magnetic properties.

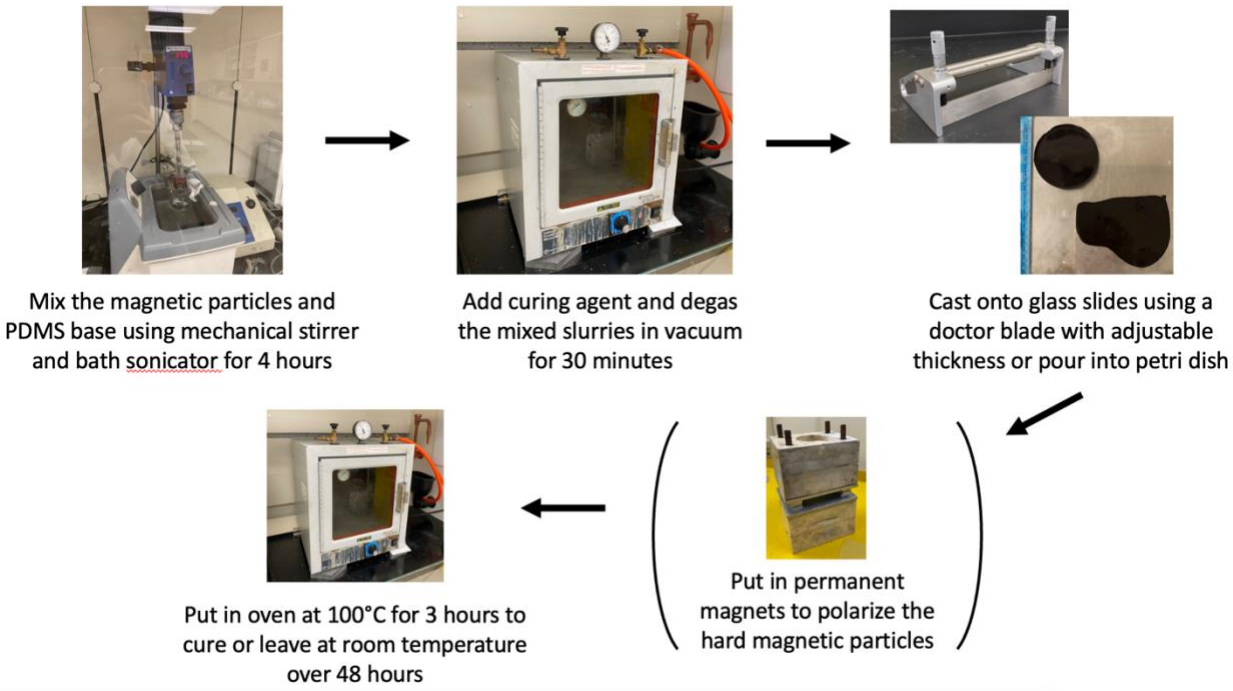

Figure 11. General fabrication processes of MAEs using PDMS as matrix.

The fabrication processes vary for BHF-PDMS and iron oxide-PDMS based on their different magnetic properties, as shown in Figure 12. For hard magnetic particles, two sets of permanent magnets were used to polarize the particles, as shown in Figure 13. One set has a field strength of 350 mT and the other set is 900 mT.

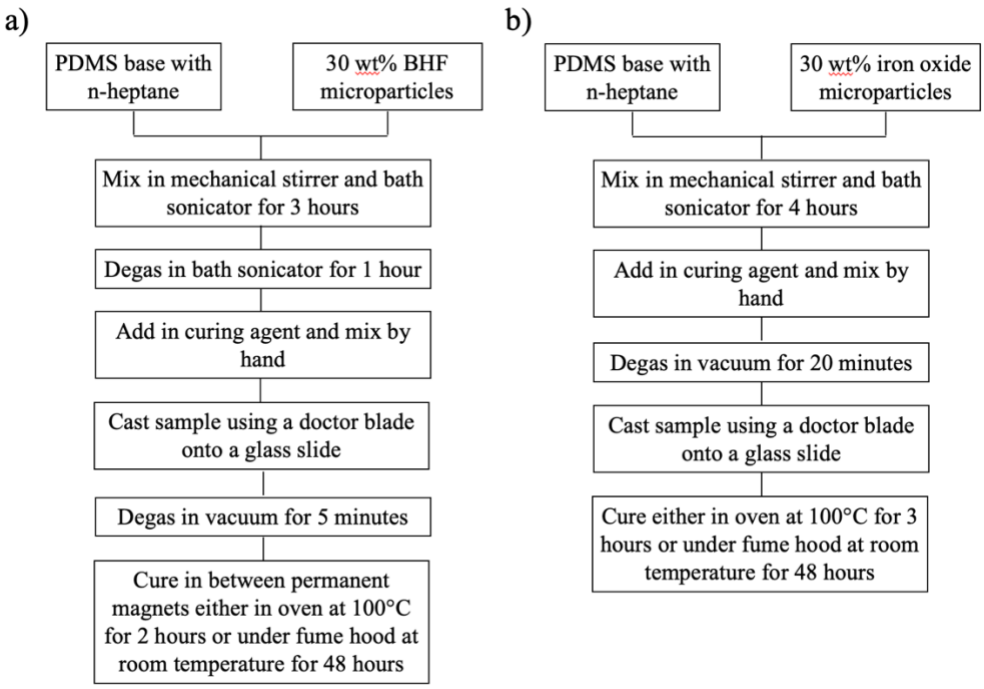

Figure 12. Flow charts showing fabrication processes for (a) BHF-PDMS and (b) iron oxide-PDMS composites.

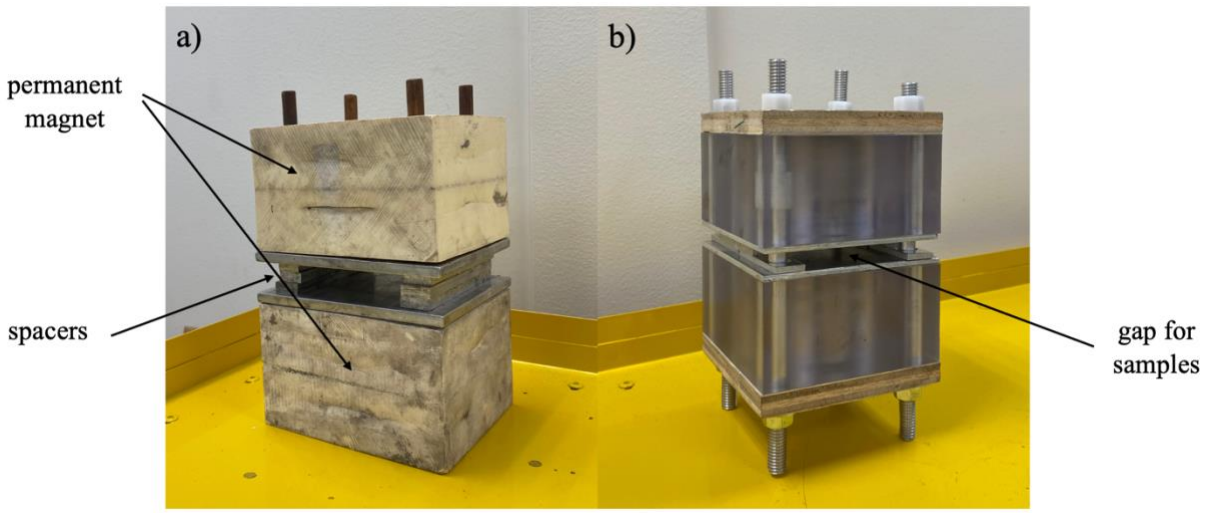

Figure 13. Permanent magnet sets used to polarize hard magnetic particles with magnetic field of (a) 350 mT and (b) 900 mT.

The fully cured MAEs were then cut into geometric shapes, such as rectangles and squares, for magnetic actuations in order to systematically study the behavior and performances of the materials. The most used dimensions of the samples were 3×1 cm thin strips, 1×1 cm and 0.5×0.5 cm squares for bending and folding actuation as shown in Figure 14. It is also important to note that for 3×1 cm actuation, a portion of the sample was fixed onto the glass slide which is shown in Figure 15, which means the active actuating length is 2.85 cm.

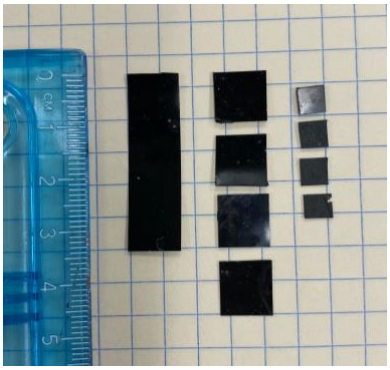

Figure 14. Cut MAE samples in various dimensions and thicknesses.

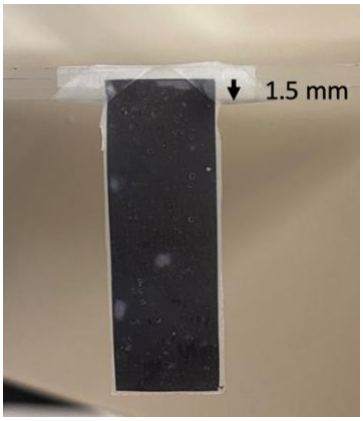

Figure 15. A 3×1 cm MAE thin strip being fixed onto a glass slide.

Similar fabrication processes were applied to iron-oxide PVA samples. PVA pellets (Alfa Aesar) were dissolved in distilled water in 12wt% using a hot plate (Corning, PC-420D) and magnetic stirrer. Figure 16 shows the fabrication setup where the beaker containing the PVA solution was submerged in a silicone oil bath (Clearco Products Co., Inc) which was maintained at 90°C using a temperature probe to expedite the mixing process. The magnetic stirrer was set at 400 rpm and the PVA pellets were slowly added into the solution over the entire course of mixing to avoid large clustering. After an hour of continuously mixing the solution, the beaker was sealed using plastic wrap (Bemis™ Parafilm™ M) and aluminum foil (Reynolds) and was allowed to sit overnight to allow any air bubbles to escape from the solution. Similar procedures as MAEs were followed by fabricating iron oxide-PVA as shown in Figure 17. It is important to note that weight percentage (for examples, 30wt% of iron oxide) is calculated based on the weight of PVA, where PVA is 70wt%. As a result of water evaporating, iron oxide-PVA thin films had a thickness around 0.05-0.1 mm which was significantly thinner than iron oxide-PDMS around 0.3-0.5 mm.

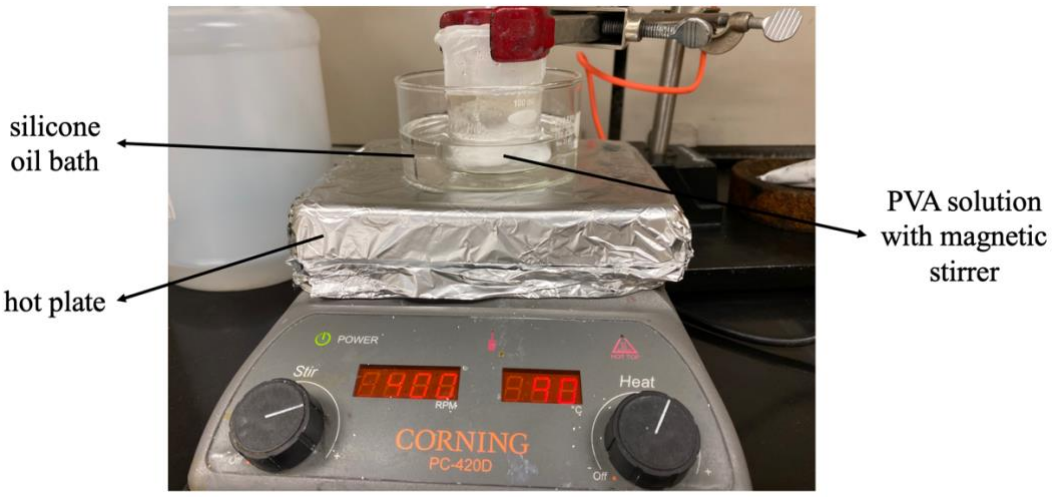

Figure 16. Setup of fabrication of PVA solution.

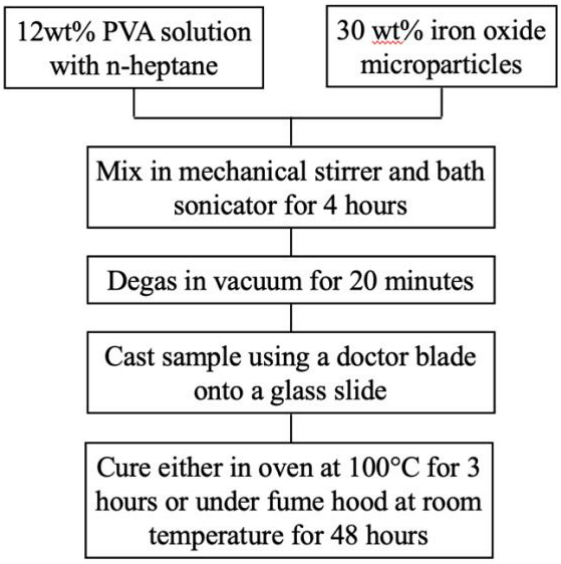

Figure 17. A flowchart showing fabrication processes of iron oxide-PVA composites.

Various actuation configurations were designed and a table summarizing the magneto-active polymer-based materials and their geometries and particle weight percentages was shown in Table 2. Actuations including bending, folding into "V" and "S" shapes and gripping were demonstrated using 30wt BHF-PDMS films. Four different weight percentages of iron oxide-PDMS at 5, 10, 20, and 30wt% were tested in bending, gripping and flower blooming configurations. A different matrix with PVA was also investigated in bending actuation using 30wt% iron oxide-PVA. Further details on sample dimensions in each actuation configurations are included in Chapter 3 and 4.

Table 2. A summary of materials fabricated with their unique actuation configurations and material compositions.

Materials	**Sample geometries**	**The amount of magnetic particles in the solid composite**

BHF-PDMS	Bending, folding “V” and “S” shapes, gripping	30wt%
Iron oxide-PDMS	Bending, gripping and flower blooming	5, 10, 20, 30wt%
Iron oxide-PVA	Bending	30wt%

2.2.2 Fabrication of SMPs and MAE-SMP composites

To fabricate a thin film of the SMP, the base and the curing agent in a volume ratio of 4:1 were stirred using a single-time-use mixing stick, as shown in Figure 18. The mixing needs to be under 20 seconds as the mixture starts to harden and reach gelation within 1 minute. The casting process of the solution is the same with MAEs using the doctor blade or pouring onto a piece of Teflon treated film, as shown in Figure 19. It is important to note that once the epoxy hardens, it is difficult to remove it from any glassware or spatula. Thus, one-time use equipment and immediate cleaning of the tools are essential to keep the epoxy from sticking.

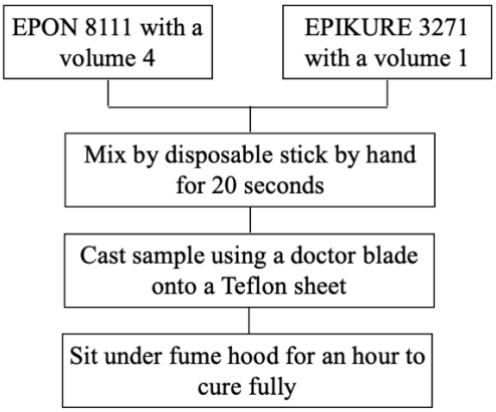

Figure 18. A flowchart showing fabrication processes of SMP composites.

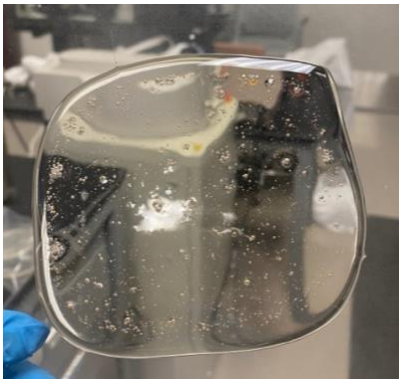

Figure 19. An SMP thin film fully cured on top of a Teflon treated film.

Samples were gathered by heating up the SMP film and using scissors to cut out 3×1 cm strips in order to match with the ones from MAEs. The heating process includes either a hot water bath using boiled water or to use a heat gun (SEEKONE 1800W) to apply hot air around the sample. The latter was more efficient as the SMP can be exposed to hot air constantly without needing to take out of the water bath and lose heat during the adjustment process.

In the initial experimenting phase, scotch tape (Magic Tape, 3M) with a thickness of 0.05 mm were used as the substrate in the unimorph structure for easier fabrication and proof of concept for MAE actuation, as shown in Figure 20. The MAE thin films were adhered to the scotch tapes with the same dimensions.

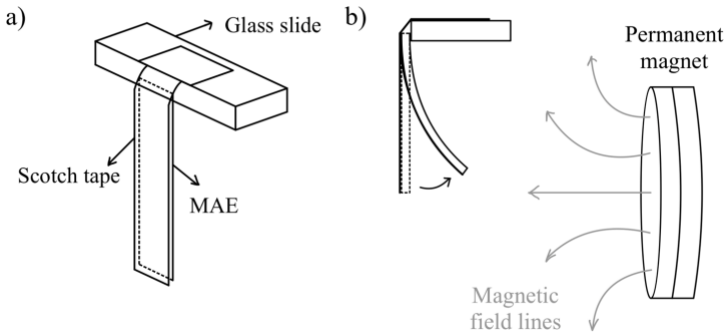

Figure 20. a) A schematic showing the setup of the unimorph structure for magnetic field actuation. Scotch tape acted as the substrate of the unimorph structure and also adhered the unimorph onto the glass slide. b) A schematic illustrating the bending actuation of the unimorph structure under external magnetic field generated by a permanent magnet. The bottom tip of the unimorph was aligned with the center of the permanent magnet horizontally at its original position.

After proving the concept of actuation, SMP thin films replaced scotch tapes in the unimorph structure to test the feasibility of multi-field actuation as shown in the schematic in Figure 21. Adhering using a double-sided tape (Scotch Indoor Mounting Tape, 3M), thin MAE and SMP films were glued together, and by actuating the MAE using an external magnetic field, SMP acted as a substrate to help enlarge the degree of actuation.

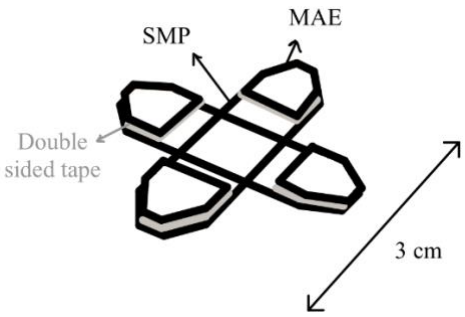

Figure 21. A designed gripping structure using MAE and SMP for gripping actuation. The double-sided tape was used for stronger adhesion in between MAE and SMP.

2.3 Characterization

2.3.1 Magnetic actuation

To assess the degree of actuation and analyze whether the designed composite structure can achieve proposed goals, different configurations for actuation were designed. Specifically, a unimorph structure that consists of a layer of active material and a layer of substrate was used in analysis of degree of actuation. The actuation setups shown in Figure 22 are different for hard and soft MAEs due to different magnetic properties. For hard magnets, an electromagnet was used as shown in Figure 22 (a), generating a uniform magnetic field in between the spacings by a DC power supply. Soft magnets, on the other hand, was actuated by moving a permanent magnet to attract the induced dipoles in Figure 22 (b).

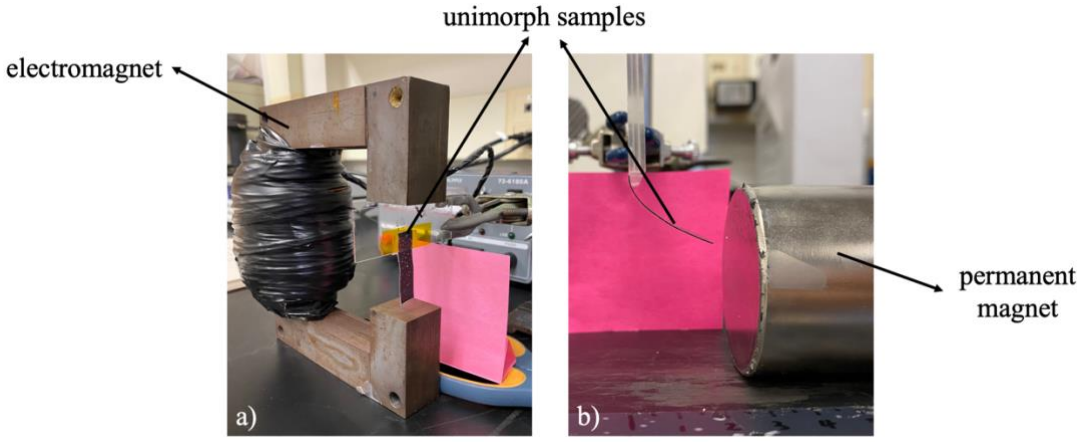

Figure 22. Actuation setup for (a) hard MAEs using electromagnet and (b) soft MAEs using permanent magnet.

The actuation mechanism for BHF-PDMS composites under the electromagnet is shown in Figure 23 and Figure 24. With the magnetic dipoles polarized in a given direction, the film reacts to external magnetic field by aligning the dipole directions with the field, i.e. a torque is

generated. Thus, by designing the direction of the magnetic dipoles in the MAEs, bending and folding actuation can be achieved.

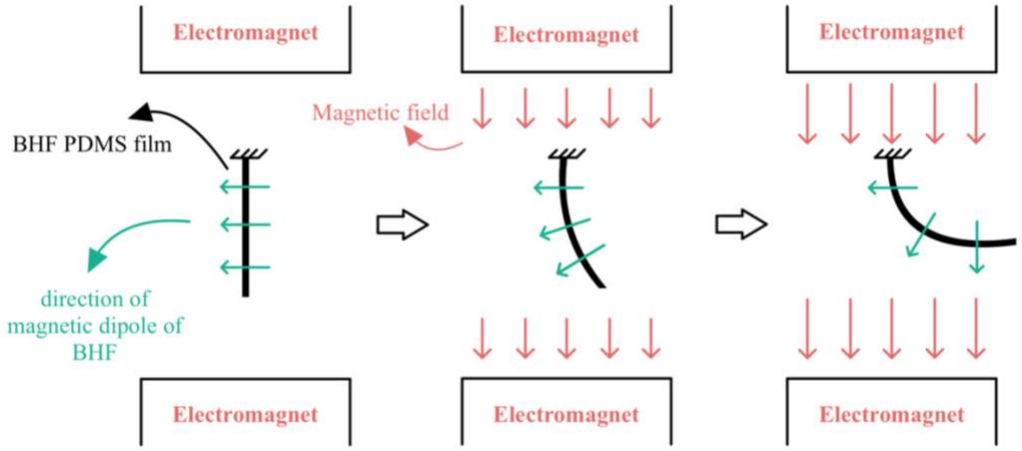

Figure 23. A schematic showing the bending actuation mechanism for BHF-PDMS, assuming the top of the film is fixed.

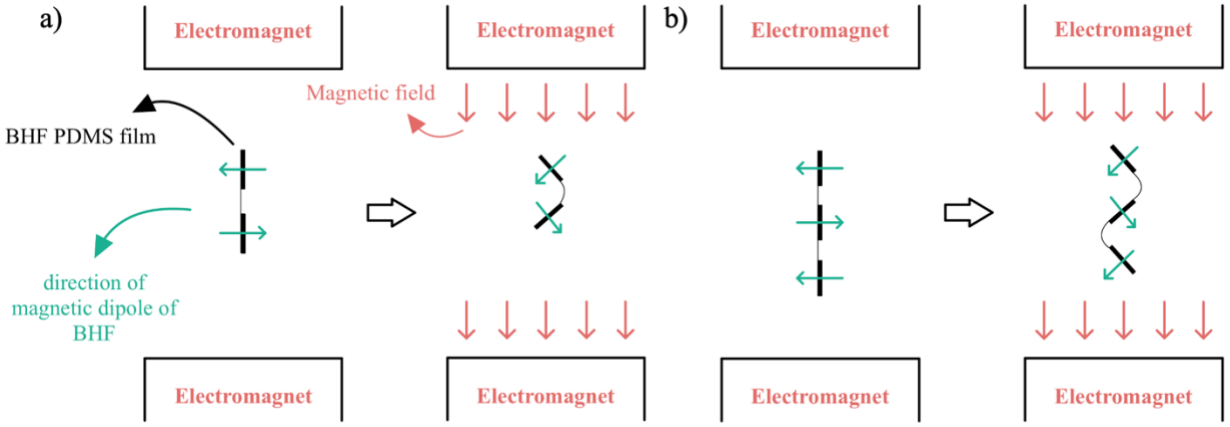

Figure 24. A schematic showing the folding actuation mechanism for BHF-PDMS with (a) one notch or (b) two notches in between specimens.

For actuating BHF-PDMS composites, the electromagnet was powered through a DC power supply, as shown in Figure 25. By changing the voltage of the DC power supply for a range of 0 V to 14.8 V, the magnetic field strength changes as well.

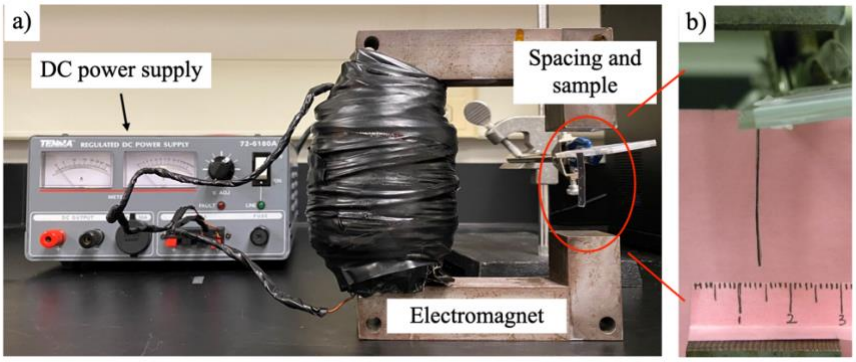

Figure 25. a) Setup of the electromagnet including the DC power supply and wires. b) The position of the sample in between the spacing of electromagnet.

To better predict actuation under external magnetic field from the electromagnet, a mapping of magnetic field was graphed. A gaussmeter (PCE-MFM 3000) was used to measure the magnetic field strength by having the detecting tip perpendicular to the field direction, and data for mapping was obtained by measuring different locations along the sample and around the actuation space. At first, an electromagnet was used to actuate BHF-PDMS due to its uniform magnetic field lines in between the top and bottom surfaces, as shown in Figure 26. The polarized BHF particles then react to the direction of the field lines and thus deform and bend. Table 3 shows the field strength along the five representative field lines. The largest field strength measured is 161 mT at the corner of the space. However, the field strength along the center of the space, which is where the sample of MAE is usually placed for actuation, only is as large as 85 mT.

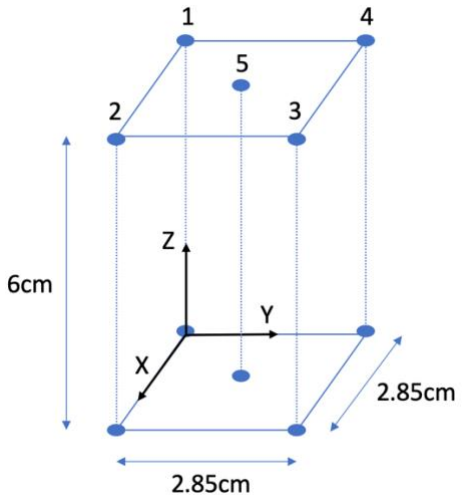

Figure 26. A schematic of dimensions and five representative field lines between the top and bottom surfaces of the electromagnet.

Table 3. A mapping of the magnetic field strength of electromagnet at the highest voltage 14V.

Z (cm)	H at 1 (mT)	H at 2 (mT)	H at 3 (mT)	H at 4 (mT)	H at 5 (mT)
0	161	143	143	140	85
0.5	83	72	79	71	77
1	59	61	60	63	67
1.5	54	51	51	55	60
2	48	46	45	49	54
2.5	45	42	42	46	50
3	45	40	41	44	50
3.5	47	42	42	45	52
4	49	44	45	49	57
4.5	54	48	50	52	65
5	60	54	58	62	74
5.5	71	62	74	74	79
6	140	144	142	132	84

The actuation mechanism for iron oxide-PDMS was different because of the soft magnetic properties. The induced dipoles only exist when external magnetic field is applied to

elicit actuation. Giving the flexibility of moving permanent magnets compared to electromagnet, the former was considered to actuate soft magnets. In order to have a greater magnetic field to achieve larger degree of actuation, permanent magnet (K&J Magnetics, Inc.) made with NdFeB with Grade N52 was considered for actuating MAEs. The cylindric permanent magnet has a diameter of 5 cm with a length of 5 cm, with magnetic field lines shown in Figure 27. Due to curved magnetic field directions, maximum local magnetic field strength was measured differently as the gaussmeter direction needs to be altered to be perpendicular to the field directions.

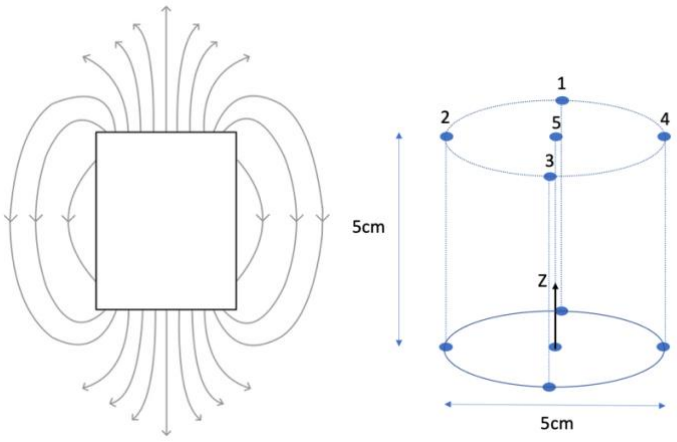

Figure 27. A schematic of the field line directions of a cylindric permanent magnet and five representative field lines for magnetic field measuring.

Considering the magnetic field, two actuation setups were specifically analyzed for the best way to actuate iron oxide-PDMS samples. A horizontal setup was designed where the sample's bottom tip was held near the center of the circular surface of the permanent magnet, as shown in Figure 28. Another setup was when the permanent magnet was positioned vertically and the sample was held above the magnet with its bottom tip near the center of the circular

surface, as shown in Figure 29. Both setups were similar for the initial position of the bottom tip, however the field directions and movements were different in the actuation process.

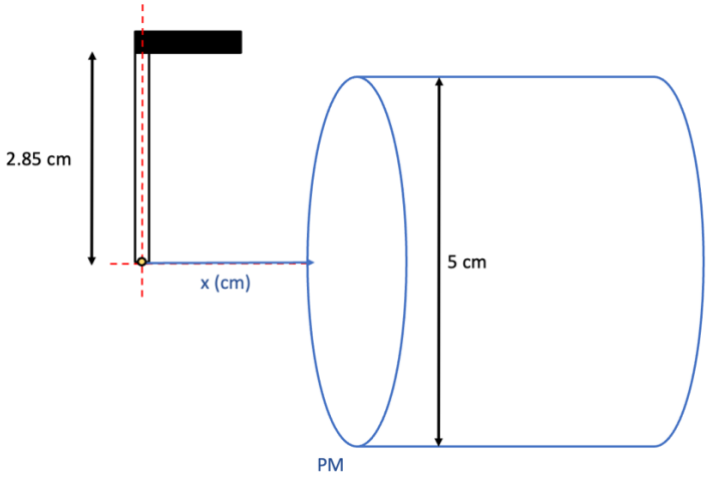

Figure 28. A schematic showing the horizontal actuation setup of iron oxide MAEs using permanent magnet.

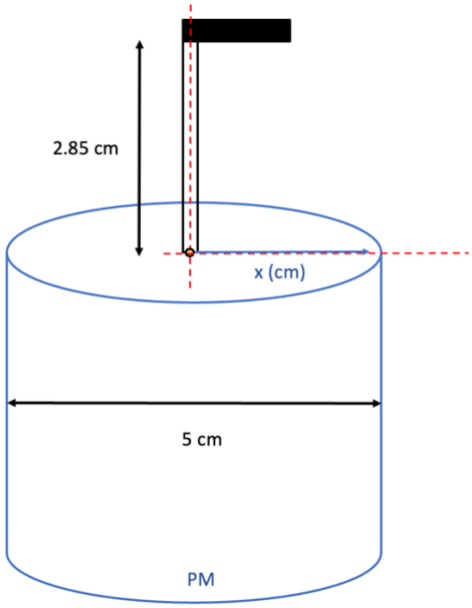

Figure 29. A schematic showing the vertical actuation setup of iron oxide MAEs using permanent magnet.

Table 4 shows the measurements measured along the diameter, which is where the sample is placed for actuation. The maximum magnetic field that can be achieved was 556.9 mT while the smallest field strength was 19.2 mT.

Table 4. Magnetic mapping of the permanent magnet on top of the circular surface.

Z (cm)	H at 1 (mT)	H at 2 (mT)	H at 3 (mT)	H at 4 (mT)	H at 5 (mT)
0	556.9	565.1	540.7	520.2	500.7
1	222.2	200.5	204.2	201.3	323.4
2	138.6	124.2	131.3	123.9	192.3
3	90.3	75.4	83.8	80.7	117.2
4	59.5	50.6	56.7	54.2	73.7
5	42.3	36.7	40.3	40.1	49.4
6	30.5	25.7	29.3	28.2	33.3
7	22.3	19.2	22	24.5	24.5

The actuation data was then collected using ImageJ. The actuation was captured into a video, and then the displacement of the sample can be tracked and measured in ImageJ. As shown in Figure 30, after setting the scale using a known object's length, measurements of displacements and angles can be taken by measuring the line drawn between two points.

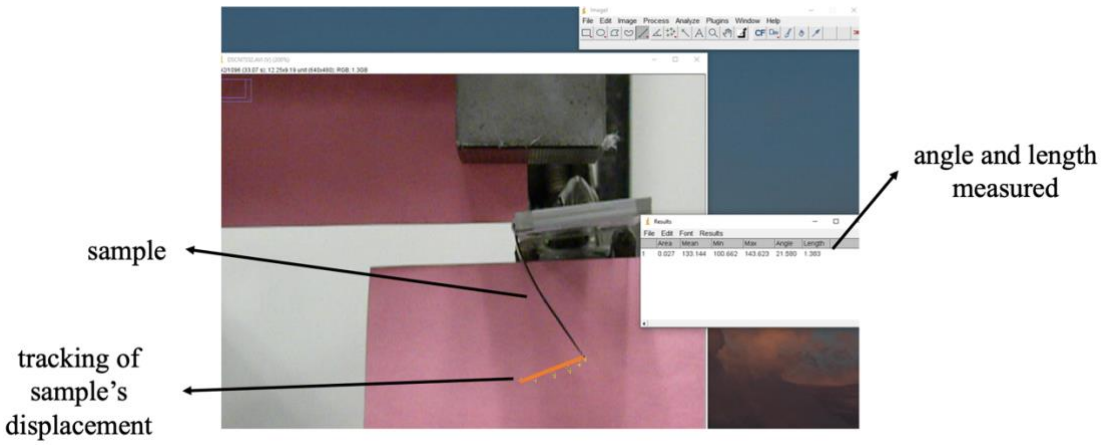

Figure 30. Demonstration of ImageJ interface when measuring actuation displacements and angles

Additionally, blocked force was measured to characterize BHF-PDMS further. Blocked force is the force generated from the sample being blocked from actuating. A force probe (Shimpo FGV-XY) was used with the tip of the probe pointing at the bottom tip of the sample with a distance of 1 mm, as shown in Figure 31. As the magnet moves, the sample will deform against the measuring tip and exert the blocked force to the measuring tip. Different ways to measure the field strength was studied as well as the field direction was curved in most places, which indicated that the tip of the gaussmeter needed to rotate as the field direction change so they stayed perpendicular to each other in order to measure the maximum magnetic field strength at each location. Since the force probe was measured horizontally It is important to note that the magnet was attracting the force gauge thus affecting the readings. Thus, a solution was come up with where the readings without sample being present was collected and subtracted by the readings with sample being present to measure the actual blocked force.

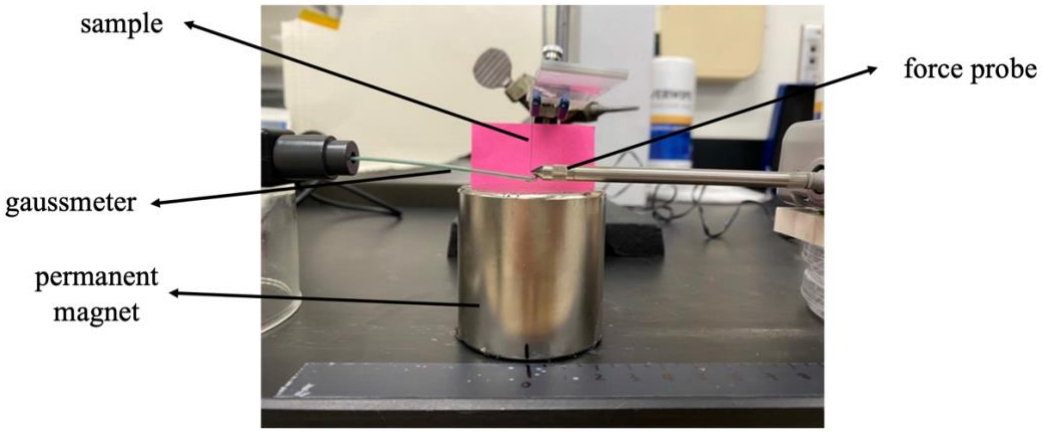

Figure 31. Setup to measure blocked force exerted by the MAE sample actuated by permanent magnet.

2.3.2 Printability

Printability was tested with iron oxide-PDMS slurries. The slurries were fabricated the same procedures as the cured composites, but without casting and heating in the oven as replaced by printing with a syringe onto a heated surface. Fumed silica powder (99%, McMASTER-CARR) was also introduced as the thickening agent for the solution, which was studied for printability using a syringe with the outlet diameter of 2.1 mm (Figure 32).

Figure 32. Manual printing by extrusion through a syringe.

Both slurries with and without the addition of fumed silica were tested by slowly pushing through the syringe on a Teflon treated film into a thin line. Hot plate was heated to 100°C to expedite the curing of printed MAEs as shown in Figure 33. The local temperature on the hot plate was measured at different locations and multiple layers of printed MAEs were experimented as well as shown in Figure 34.

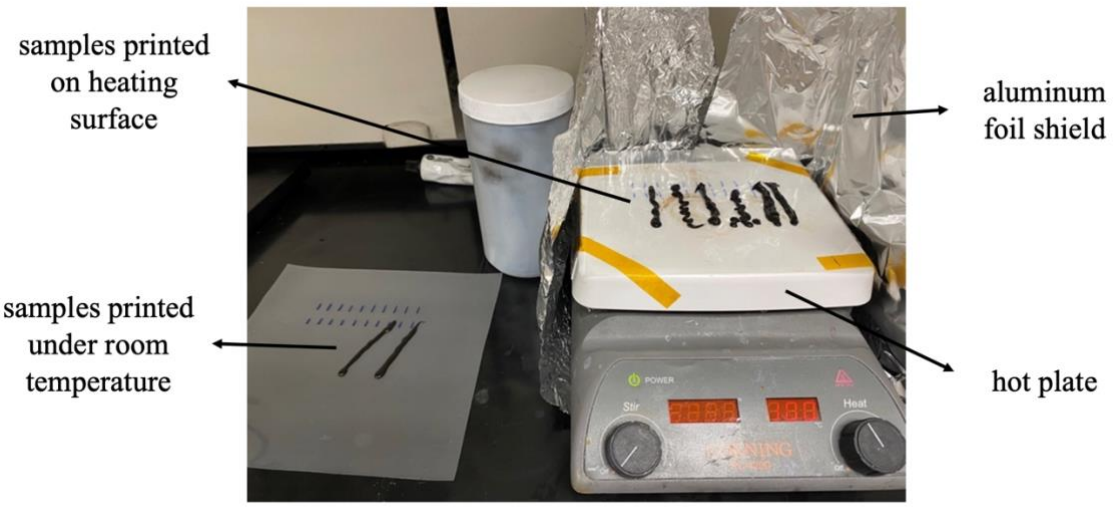

Figure 33. Setup of printability test. Aluminum foil walls were applied to contain heat within the area.

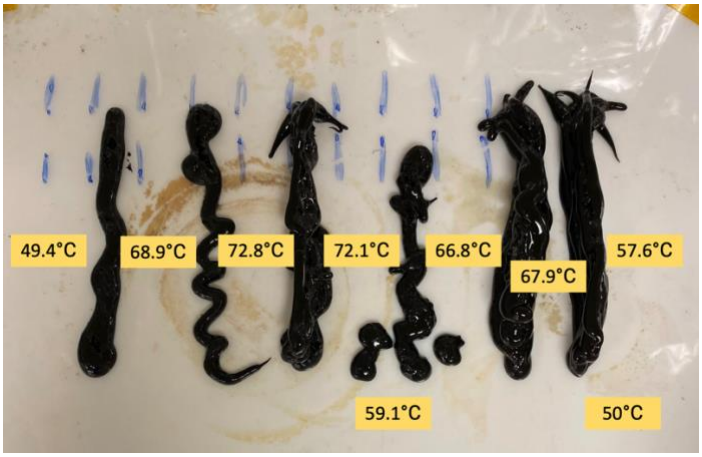

Figure 34. Printed MAE thin lines on top of the hot plate with temperature measured at different locations showing non-uniform heating.

2.3.3 Vibrating sample magnetometry (VSM)

In order to determine the magnetic properties of the magnetic particles, vibrating sample magnetometry (VSM) was performed on both magnetic microparticles and magneto-active

polymer-based composites. The samples were placed in a uniform magnetic field which induced a magnetic moment in the samples. A sinusoidal motion in the field was applied onto the sample and sensing coils around the sample then measured the magnetic flux density, where a relationship between the magnetization of the sample and the applied field can be achieved from. A hysteresis loop is then plotted to present the data. The saturation magnetization, which is the highest magnetization detected from the sample, was then compared between samples to analyze the magnetic properties. Along with the saturation magnetization, coercivity and remanent magnetization can be observed to determine hard and soft magnetic properties.

2.3.4 Dynamic mechanical analysis (DMA)

The mechanical properties of hard MAEs were characterized through tensile tests using a dynamic mechanical analyzer. Samples for the tensile tests were cut into 1×4 cm and 4-5 samples were prepared for each batch of samples for accuracy. The samples were elongated at a rate of 5 mm/min with a maximum force of 48 N. The amount of force applied on to the sample until breakage was recorded every 0.1 second. Stress values were calculated with force divided by cross section area, and strain values were calculated using the crosshead length measured divided by the width of the sample. A stress strain curve was then obtained to calculate Young's modulus using the slope of the elastic portion of the curve, which assessed the elasticity of the materials.

2.3.5 Differential scanning calorimetry (DSC)

DSC (TA instruments model Q-2000) was conducted on iron oxide-PVA samples to analyze the thermal properties, such as glass transition temperature T_g and heat flow during the

heating process of polymers. During the characterization, two aluminum pans are heated at a constant temperature ramp rate, one being the sample and one being the reference (empty) pan. The heat flow shows differences when the polymer goes through a thermal transition compared to the reference pan. Both aligned and unaligned iron oxide-PVA and pure PVA were tested at both 10°C/min and 20°C/min for 2 cycles from 0°C to 300°C.

2.3.6 Optical microscopy (OM)

To investigate whether there is any patterns or agglomerations in the MAEs, optical microscopy (ZEISS) was conducted on iron oxide-PDMS and iron oxide-PVA samples. Magnifications of 10× and 16× were observed and compared to note the particle dispersions. The samples were cut in thin strips with widths of 1-1.5 mm and put on a glass slide under the microscope.

2.3.7 Scanning electron microscopy (SEM)

Scanning electron microscopy was performed on iron oxide-PDMS and iron oxide-PVA samples. The films were first fractured using liquid nitrogen so that the cross-section can obtain a brittle fracture. The cross section was then sputter coated to allow conductivity and prevent charge buildup from shooting electrons. SEM was conducted to observe particle distributions and orientation across the thickness of the sample film.

Chapter 3

Actuation and printability of conventionally-cast MAEs

3.1 Magnetic actuation of BHF-PDMS

To assess the degree of actuation of conventionally-cast MAEs, a unimorph structure containing one layer of active (MAE) material and one layer of passive substrate adhered together was designed and placed in an external magnetic field. The actuation mechanism was due to magnetic dipole directions aligning with external magnetic field directions, and was explained in detail in Chapter 2 section 2.3. It is noted that the MAEs here are prepared using 30wt% BHF in PDMS. Samples of various geometries were prepared as discussed in Chapter 2 section 2.2.1 which include 0.5×0.5 cm and 1×1 cm squares, and 3×1 cm strips. Table 5 lists all the samples with their geometries and compositions that were studied. Weight percentage was calculated based on the total weight of magnetic particles and PDMS base, which means 30wt% was when magnetic particles took 30% of the total weight.

Table 5. A list of BHF-PDMS samples.

BHF-PDMS samples geometries	**Unimorph geometries**	**The amount of magnetic particles in the solid composite**
0.5×0.5 cm	S-shape folding– three pieces on a scotch tape	30wt%
1×1 cm	V-shape folding – two pieces on a scotch tape	30wt%
3×1 cm	Bending – one piece on a scotch tape	30wt%
0.5×1 cm	Gripping – three pieces on separate scotch tapes	30wt%

The magnetic actuation includes bending and folding demonstrations, and the degree of bending was quantified by measuring the displacement of the bottom tip of the unimorph, which was explained in Figure 30. Figure 25 in Chapter 2 section 2.3 explains the setup using electromagnet to generate a uniform magnetic field to actuation BHF-PDMS samples. Figure 35 shows displacement of the bottom tip with respect to magnetic field and that the maximum average displacement was found to be around 2 cm at 57 mT.

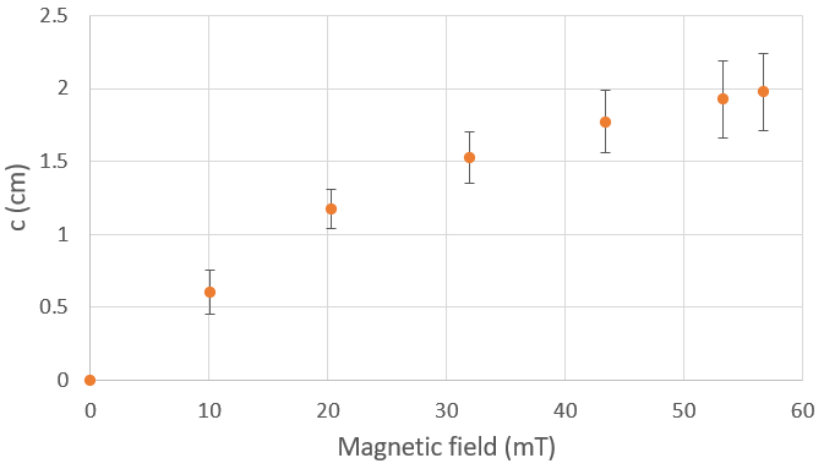

Figure 35. Actuation displacement of bottom tip of BHF-PDMS unimorph.

Figure 36 shows the actuation of a BHF-PDMS sample adhered to a layer of scotch tape. The bending actuation of the samples were compared when the samples were placed at different locations in the electromagnet. While Figure 36 (a) has the sample fixed in the center of the spacing, the bottom tip of the sample was actuated by the magnetic field outside the spacing which was significantly smaller than the field inside the spacing. Figure 36 (b) elicited a larger actuation by having the sample inside the spacing even as it actuated, resulting in larger bending.

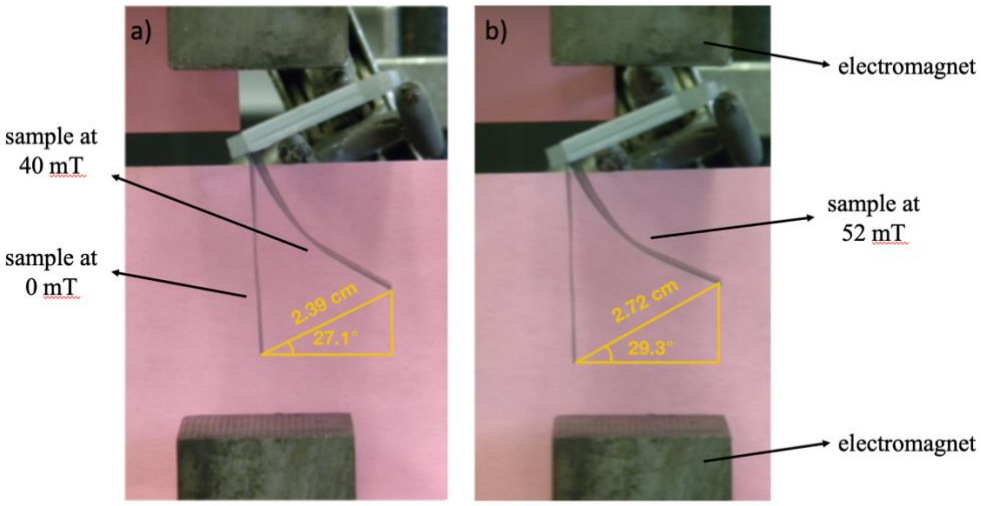

Figure 36. BHF-PDMS thin strip bending actuation when the top tip was held (a) along the centerline of the electromagnet and (b) towards the edge of the electromagnet.

Blocked force as another method to assess the effect of materials on actuation was measured for 30wt% BHF-PDMS composites. The curve as shown in Figure 37 was the average taken from 3 different samples and the maximum average was observed to be 0.02 N.

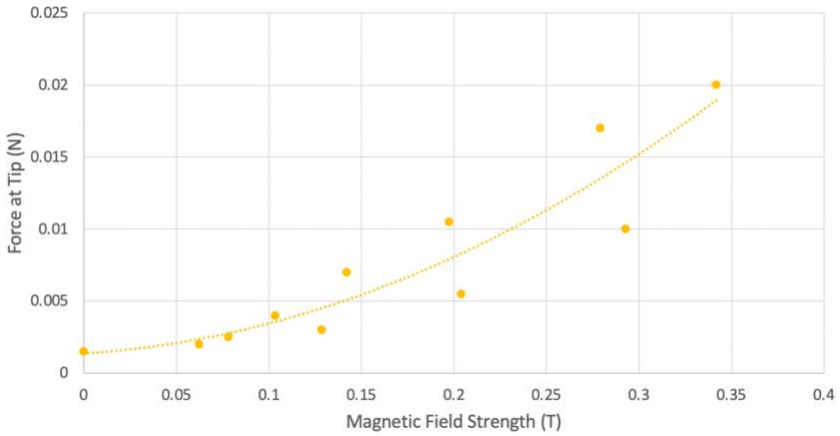

Figure 37. Blocked force measurements on 30wt% BHF-PDMS samples.

Folding actuation was also assessed by introducing notches in the BHF-PDMS samples. The unimorph is constructed using multiple MAE samples attached at different locations along the scotch tape substrate, as shown in Figure 38. Folding actuation can be achieved in a configuration where the samples' magnetic dipoles are facing opposite directions with each sample's magnetic dipole facing opposite directions. Figure 39a shows a folding actuation using two pieces of BHF-PDMS and Figure 39b demonstrates an S-shaped actuation with three pieces of BHF-PDMS. Dipole directions are indicated in the figure as well.

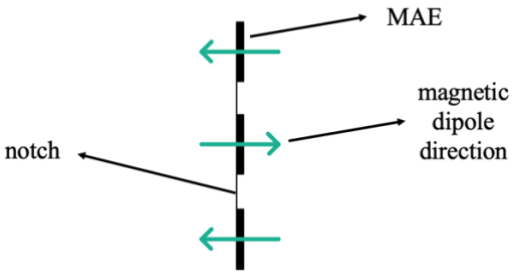

Figure 38. Schematic showing a unimorph structure with notches.

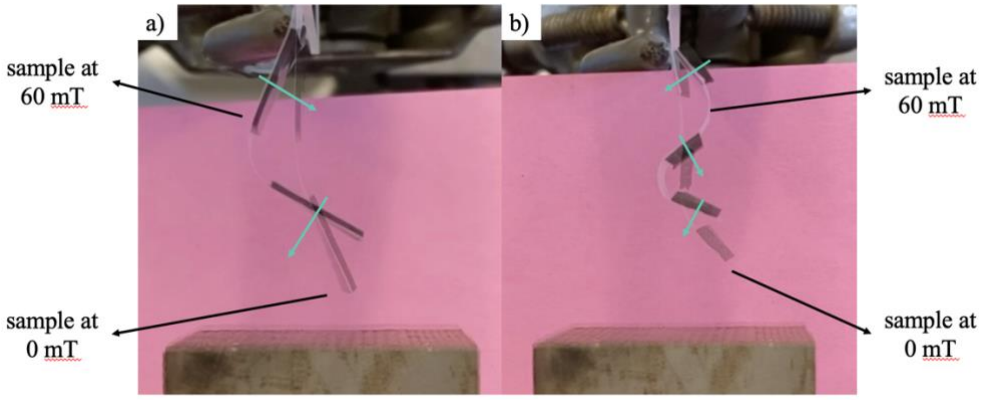

Figure 39. Folding actuation using a) two pieces of BHF-PDMS and b) three pieces of BHF-PDMS attached to one single piece of scotch tape.

Vibrating sample magnetometry (VSM) was performed on BHF powders, showing hard magnetic properties with large coercivity and remanent magnetization as expected. The saturation magnetization is about 53 emu/g.

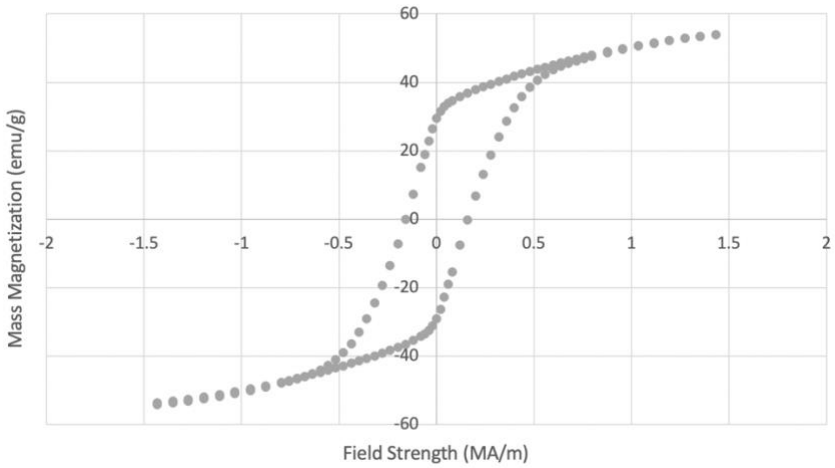

Figure 40. Hysteresis loop of BHF microparticle powders.

Hysteresis loops of fabricated 30wt% BHF-PDMS composites were also gathered and shown in Figure 41. Large coercivity and remanent magnetization were observed from BHF-PDMS composites. The saturation magnetization of the BHF-PDMS composite is around 50 emu/g, which is slightly smaller the BHF powders. This result is expected since the same BHF powder was used in both cases.

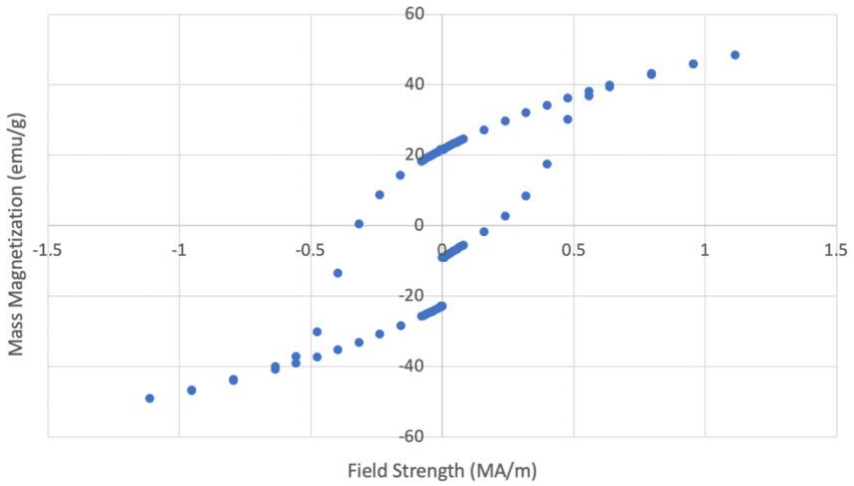

Figure 41. Hysteresis loops for 30wt% BHF-PDMS composites.

Tensile tests conducted on BHF-PDMS were conducted. Figure 42 shows the stress-strain curves calculated from the samples. The fitted line showed Young's modulus through the slope, and that of BHF-PDMS is 2.48 MPa. It is important to note that both oven cured and room temperature cured samples showed similar tensile strength with the same materials and polarization patterns.

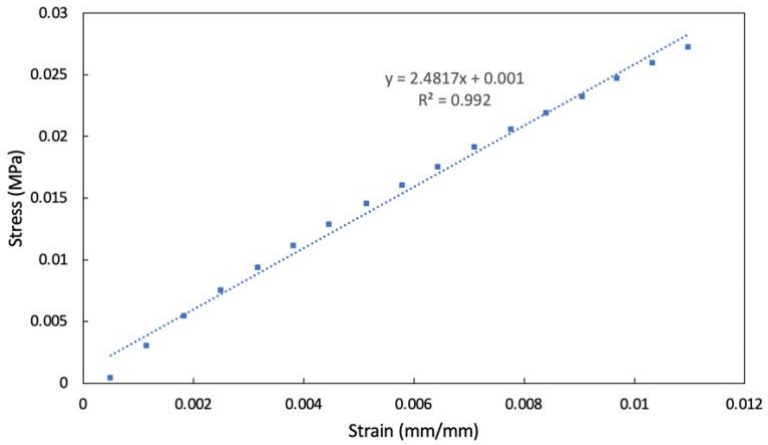

Figure 42. The stress-strain curves of BHF-PDMS thin films.

3.2 Magnetic actuation of iron oxide-PDMS

The degree of actuation of iron oxide-PDMS composites were assessed. Two compositions of 5wt% and 30wt% were fabricated and studied and the geometries studied are shown in Table 6. The fabrication processes were discussed in Chapter 2 section 2.2.1.

Table 6. A list of iron oxide-PDMS samples.

Iron oxide-PDMS samples geometries	**Unimorph geometries**	**The amount of magnetic particles in the solid composite**
1×1 cm	Bending in functional gradient – three pieces on a scotch tape	10, 20, 30wt%
3×1 cm	Bending – one piece on a scotch tape	30wt%
0.5×1 cm	Gripping – two pieces on separate scotch tapes	30wt%
3×1 cm	Flower blooming – two pieces on separate scotch tapes	5, 30wt%

The actuation setup used a permanent magnet to attract the induced dipoles in iron oxide, which was explained in detail in Chapter 2 section 2.3. As the permanent magnet moves closer to the sample, a greater actuation was elicited and magnetic field applied to the bottom tip of the sample at different locations was measured as shown in Figure 43. Displacement measurements were recorded and are shown in Figure 44. The measurements indicate that the larger the field strength was, the larger the degree of actuation was achieved.

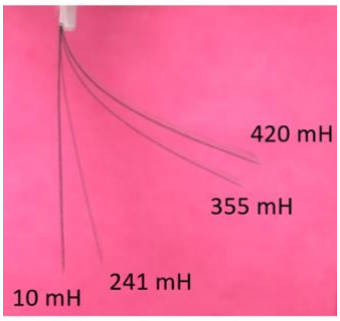

Figure 43. Different degrees of actuation at different external magnetic field.

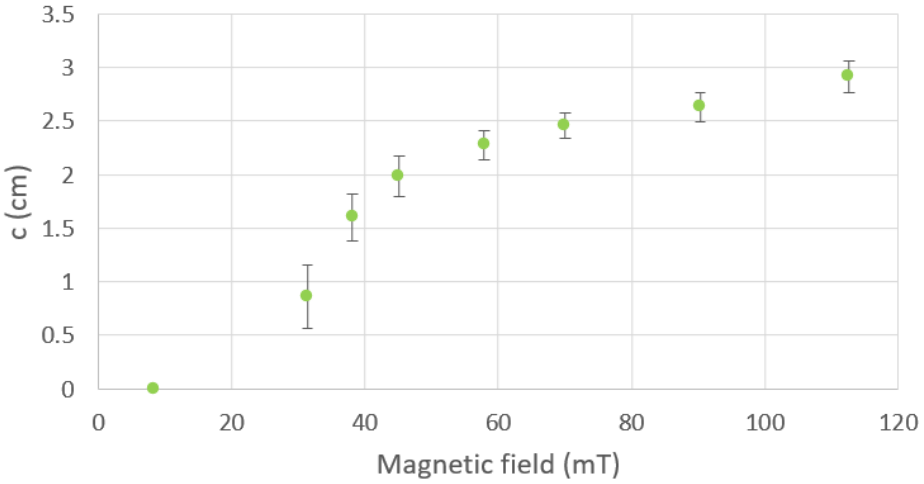

Figure 44. Actuation displacement of bottom tip of iron oxide-PDMS unimorph.

From vibrating sample magnetometry (VSM) performed on iron oxide powders, Figure 45 shows the hysteresis loops of both sieved and unsieved iron oxide microparticles. It is important to note that sieving the particles to be more dispersed without agglomeration slightly increased the saturation mass magnetization. Iron oxide particles showed soft magnetic properties with no coercivity and remanent magnetization as expected.

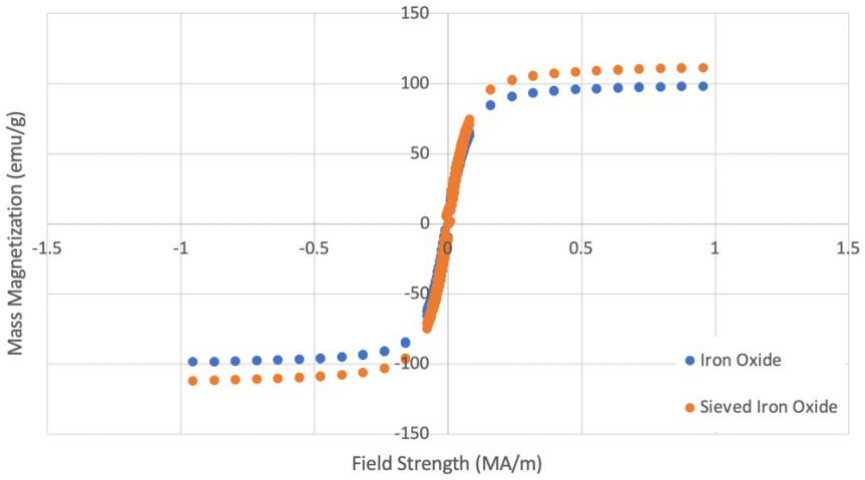

Figure 45. Hysteresis loops of original and sieved iron oxide microparticle powders.

Hysteresis loops of 30wt% iron oxide-PDMS composites were compared for magnetic properties as shown in Figure 46. In order to measure precise weight of the iron oxide particles inside the composites, stacked samples and using more precise weighing scales were both implemented. Figure 46 shows the hysteresis loops for 3, 5 and 30wt% iron oxide-PDMS, where the curves of 5 and 30wt% were overlapping and the saturation magnetization of 3wt% was lower than both 5 and 30wt%. The average saturation magnetization is significantly lower compared to iron oxide powder shown in Figure 45. It is also important to note that the saturation magnetization for iron oxide-PDMS composites is smaller than iron oxide powder. Comparison between BHF and iron oxide was observed and that iron oxide powder and iron oxide-PDMS composites both have a larger saturation magnetization around 90-100 emg/g than both BHF powder and BHF-PDMS composites as previously shown in Figure 40 and Figure 41.

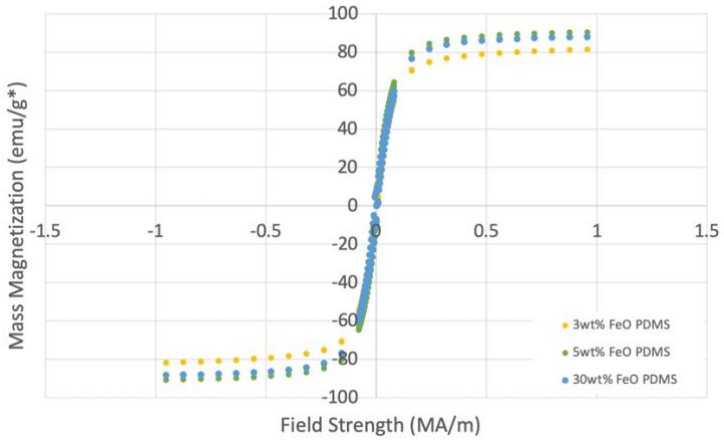

Figure 46. Hysteresis loops for 3, 5, and 30wt% iron oxide-PDMS composites.

Tensile tests on iron oxide-PDMS were conducted and shown in the stress-strain curve in Figure 47. The Young's modulus from the slope of the line is calculated to be 1.66 MPa, which is lower than that of BHF-PDMS. The Young's modulus for both materials indicated possibilities of alignment of the particles affecting the strength of the BHF-PDMS composites.

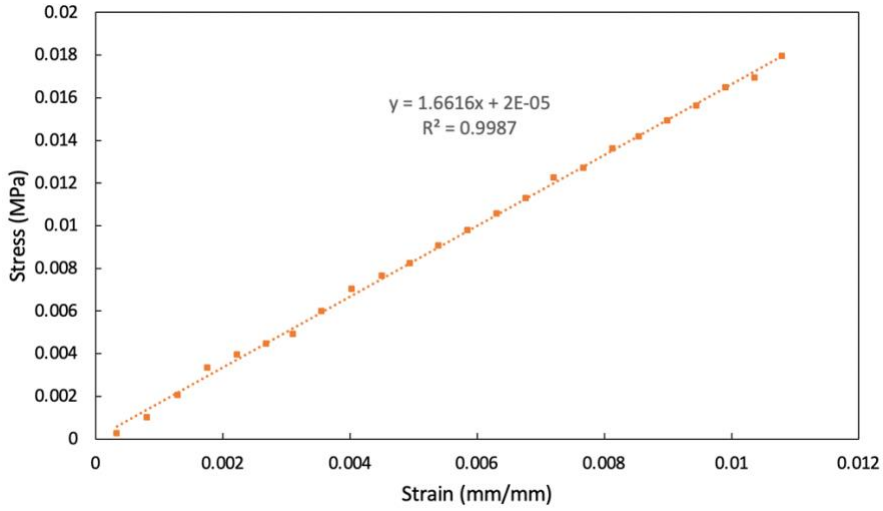

Figure 47. The stress-strain curves of iron oxide-PDMS thin films.

Optical microscopy (OM) was conducted on iron oxide-PDMS samples with various weight percentages of 3, 5, 10, 20, and 30. All MAE films were cut into thin strips with thicknesses around 0.25 mm and observed under a magnification of 10×. Figure 48 shows the OM of 3wt% iron oxide-PDMS, where visible iron oxide microparticles was noticed, which could be due to the little amount of iron oxide microparticles inside the matrix.

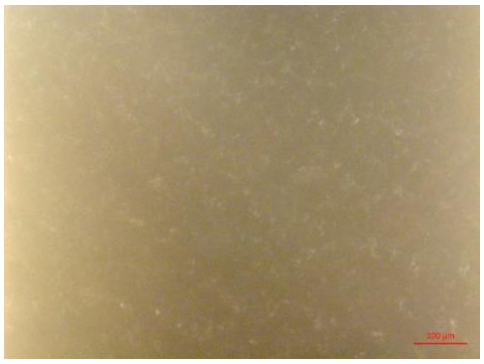

Figure 48. OM on 3wt% iron oxide-PDMS samples.

3.3 Demonstration of more complex actuation shapes

Other designs of geometries and configurations based on MAE-scotch tape unimorph structures were also experimented with, such as a 4-finger gripper which is shown in Figure 49. The structure was designed by attaching two pieces of iron oxide-PDMS composites on two ends of a scotch tape strip and combining two sets of these into a 4-finger gripper configuration. The center of the composite was adhered to a hard surface so that the whole piece stays unmoved. As the permanent magnet moved closer to the gripper from above, the external magnetic field elicited actuation of the fingers to perform a gripping motion.

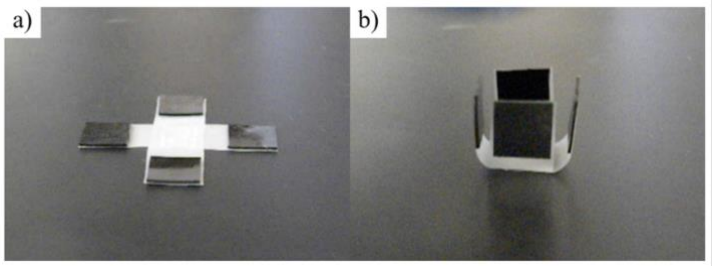

Figure 49. Gripping actuation of soft MAEs showing (a) with no external magnetic field b) with external magnetic field applied.

Actuation configurations combining multiple materials as well as different material compositions were studied as well. As shown in Figure 50, a gripping configuration using both 30 wt% hard and soft MAEs, which were BHF-PDMS and iron oxide-PDMS, was actuated by moving the permanent magnet closer from underneath. The three BHD-PDMS fingers first closed together as poled BHF microparticles aligned with the external magnetic field directions. As the permanent magnet moved even closer, the two iron oxide-PDMS fingers on the side deformed downwards due to induced dipoles in iron oxide microparticles.

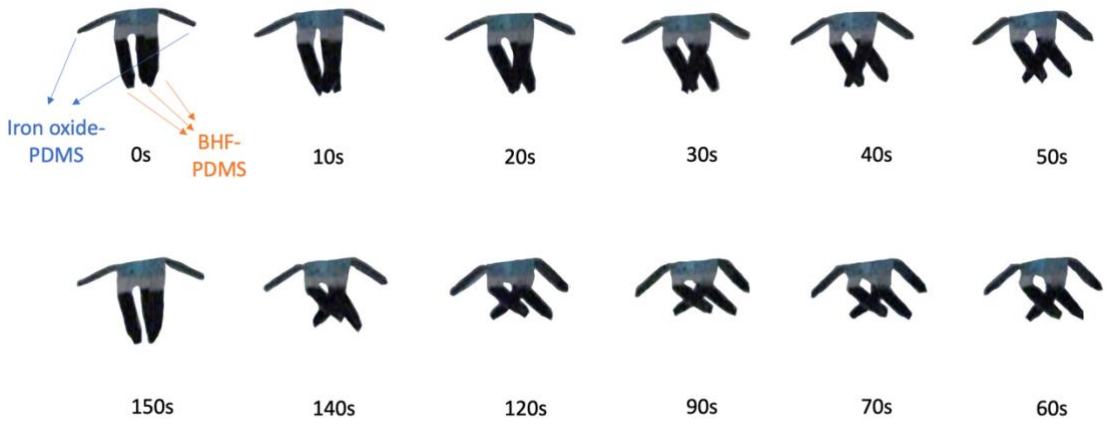

Figure 50. Actuation of a gripping configuration consisting of both hard and soft MAEs.

Different weight percentages of iron oxide-PDMS were also combined into a gripping configuration for different actuation responding rate and degree of bending as shown in Figure 51. The less the weight percentage of particles was in the iron oxide-PDMS, the slower and smaller actuation was achieved. The experiment showed that the 30wt% fingers first were actuated downwards in the first six seconds of moving permanent magnet closer, and then the 5wt% fingers started bending as the magnetic field increased even more.

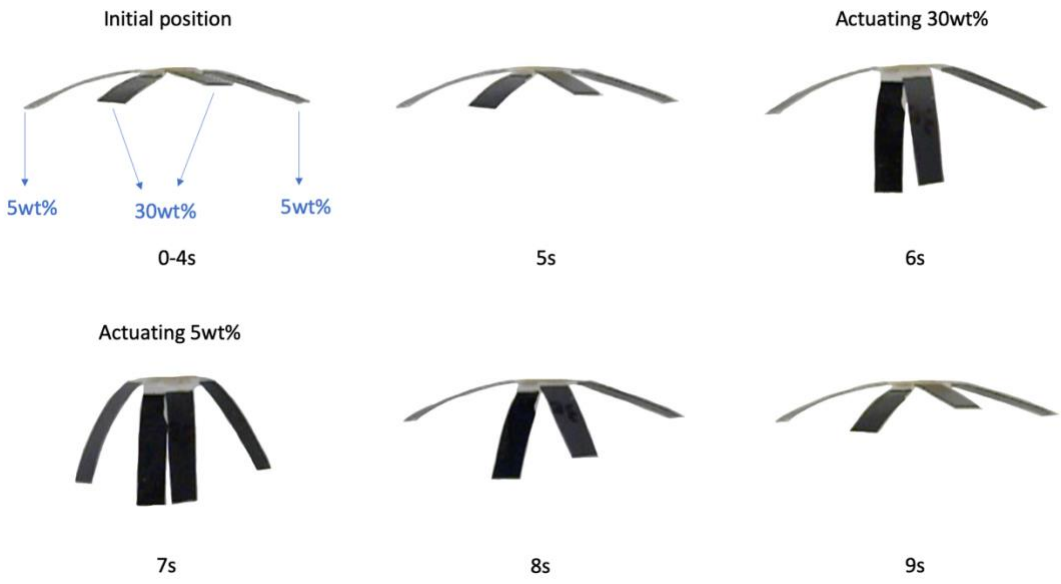

Figure 51. Actuation of various weight percentage of soft MAEs.

Functional gradient in the MAEs was also experimented with. Different weight percentages of iron oxide-PDMS composites were adhered to one single substrate of scotch tape, and put under external magnetic field for actuation comparison. In this experiment, 10, 20 and 30wt% iron oxide-PDMS thin films cut in 1×1 cm squares adhered to scotch tape was investigated. The degree of actuation was different as the order of the MAE squares was

switched, as shown in Figure 52. Part (a) showed a larger curvature on top and straighter line at the bottom, which indicated a larger force was exerted by actuating the 30wt% MAE at the bottom. On the other hand, part (b) showed more curvature at the bottom, indicating the force exerted from the 10wt% MAE was not as strong as the 30wt% MAE on top. It is also important to note that different degrees of tilting were observed from bending actuation as shown in Figure 36, Figure 43, and Figure 52. The samples deformed with an angle of rotation, which was mainly due to the geometries of the samples from cutting manually and also the use of scotch tape could lead to un-uniform structure.

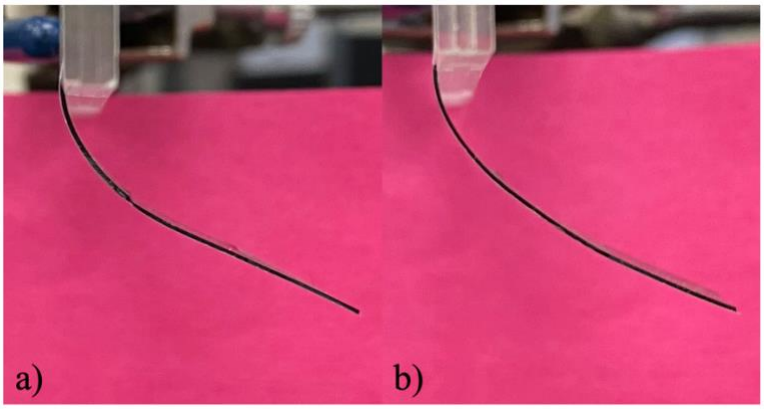

Figure 52. Actuation of functional gradient structures using 10, 20, 30wt% iron oxide-PDMS with (a) 10wt% on top, 20wt% in the middle and 30wt% at bottom and (b) 30wt% on top, 20wt% in the middle and 10wt% on bottom.

3.4 Printability

Printability was studied in order to explore additive manufacturing of MAEs to achieve more complex geometries and higher qualities of products. 30wt% iron oxide-PDMS slurries were selected to represent MAEs and printability was tested. A syringe test was implemented as explained in Chapter 2 section 2.3. The results are summarized in Table 7 which shows a comparison of the average gelation time and spreading of different compositions of iron oxide-

PDMS slurries. During gelation, we monitored the temperature of the hot plate surface, which varied from 50°C to 70°C as discussed in Chapter 2 section 2.3, indicating non-uniform heating as there was a u-shaped heating tube underneath the hot plate platform. The width of the printed lines was measured to monitor the extent of spreading of the slurries following extrusion from the syringe. In Table 7, the lower value of spreading is the minimum amount of spread along a line after extrusion, and the higher value is the maximum. The results from 6:1 PDMS base to curing agent ratio showed no significant difference from 10:1 ratio tests based on the gel time and spreading measurement. The gel time of 10:1 ratio is showing the best results being the fastest among the three, however, the addition of fumed silica increased the viscosity of the slurries and improved the ability of the extruded slurry to maintain its shape based on its spreading measurement being significantly smaller than the other two tests. The viscosity of the MAE without fumed silica was measured using a rotational viscometer (Anton Paar), and the results are recorded in Table 8, confirming the conclusion that the addition of fumed silica increased the viscosity of the MAE.

Table 7. A summary of gelation times for three different batches of MAE slurries printed on top of the hot plate at 50-70°C

Iron oxide-PDMS samples	**Number of layers printed**	**Average gel time (min)**	**Spreading measurement (mm)**
6:1 PDMS base to curing agent ratio	3	8	1 – 13
10:1 PDMS base to curing agent ratio	8	6.6	1 – 13
10:1 PDMS base to curing agent ratio, with 5 wt% fumed silica	8	7.7	0 – 3

Table 8. The viscosity of the MAE formulation with various amounts of added fumed silica with weight percentages based on the weight of PDMS base [36].

MAE			
Wt.% Fumed Silica	0	2	3.5
Viscosity (Pa*s)	too low	2.64	6.72

In order to assess the influence of fumed silica being added on actuation of iron oxide-PDMS composites, comparison between samples without fumed silica and samples with 5wt% fumed silica added was conducted, as shown in Figure 53. The data representing different samples mostly clustered together with no significant differences.

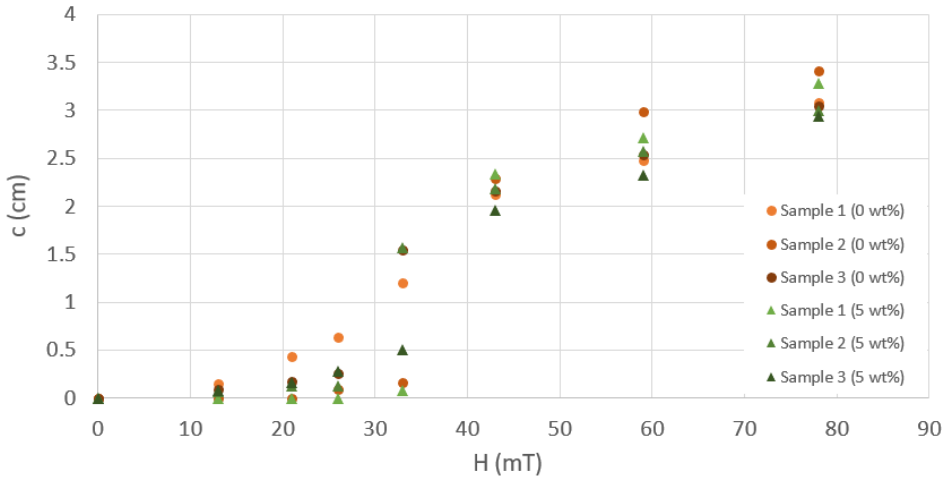

Figure 53. Actuation displacement of the bottom tip of the samples compared with or without fumed silica.

Chapter 4

Effects of matrix type on actuation

4.1 Comparison of displacement

To test the effect of changing matrix on magneto-active polymer-based materials with different mechanical properties, PVA was selected for comparison with PDMS matrix. Particularly, the magnetic particles used in both matrices were iron oxide microparticles. The details in material processing were described in Chapter 2 section 2.2.1. Table 9 shows the sample geometries and unimorph structures of iron oxide-PVA studied.

Table 9. A list of iron oxide-PVA samples.

Iron oxide-PDMS samples geometries	**Unimorph geometries**	**Compositions**
3×1 cm	Bending – one piece on a scotch tape	30wt%

First, actuation was demonstrated and measured with 30wt% iron oxide-PDMS and iron oxide-PVA thin films separately. Due to the different thicknesses of the composites, the actuation displacement was further normalized by dividing by the thickness of the composite films and the EI, which is Young's modulus times moment of inertia, of the composite. The Young's modulus were extracted from tensile test results showing in Figure 47 and Figure 56. Moment of inertia was calculated using sample width b and thickness h with the equation of $I = \frac{bh^3}{12}$ for rectangles. The resulting data is shown in Table 10.

Table 10. Young's modulus and moment of inertia of 30wt% iron oxide-PDMS and 30wt% iron oxide-PVA for data normalization.

Material	E (Pa)	b (cm)	h (cm)	I (cm^4)	EI (Pa*cm^4)
Iron oxide-PDMS	1661600	1	0.015	2.8125E-07	0.467325
Iron oxide-PVA	1895200000	1	0.005	1.0417E-08	19.74166667

Figure 54 shows the comparison between the bottom tip displacements of the samples in the horizontal setup, as all data was taken from the averages gathered using five samples of each material. Figure 55 shows the comparison in the vertical setup with the same methods of data normalization. Most of the measurements indicate that iron oxide-PDMS had a larger actuation. Both thickness normalized data in horizontal and vertical setups show a drastic decrease in the difference between two materials, particularly the vertical setup data in Figure 55 (c) shows the opposite where iron oxide-PVA has a higher displacement, which is indicating the effect of thickness on actuation.

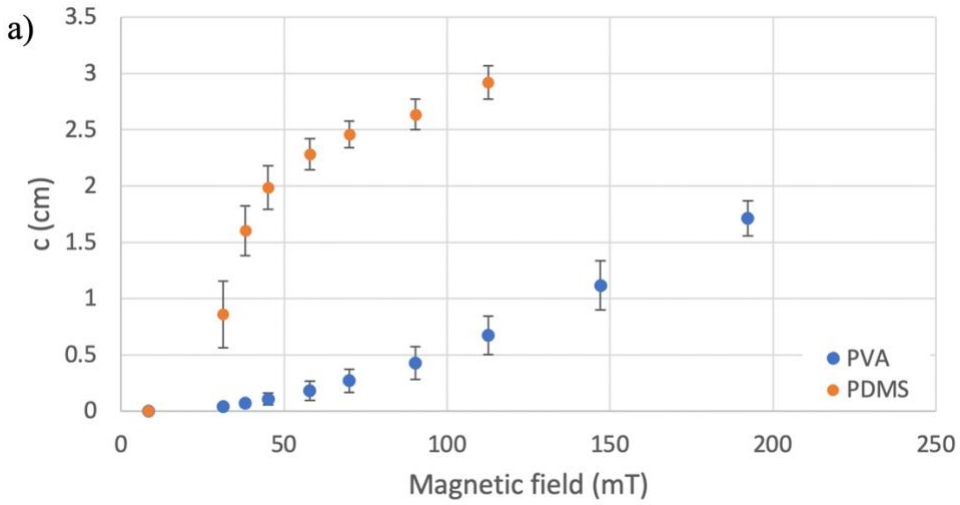

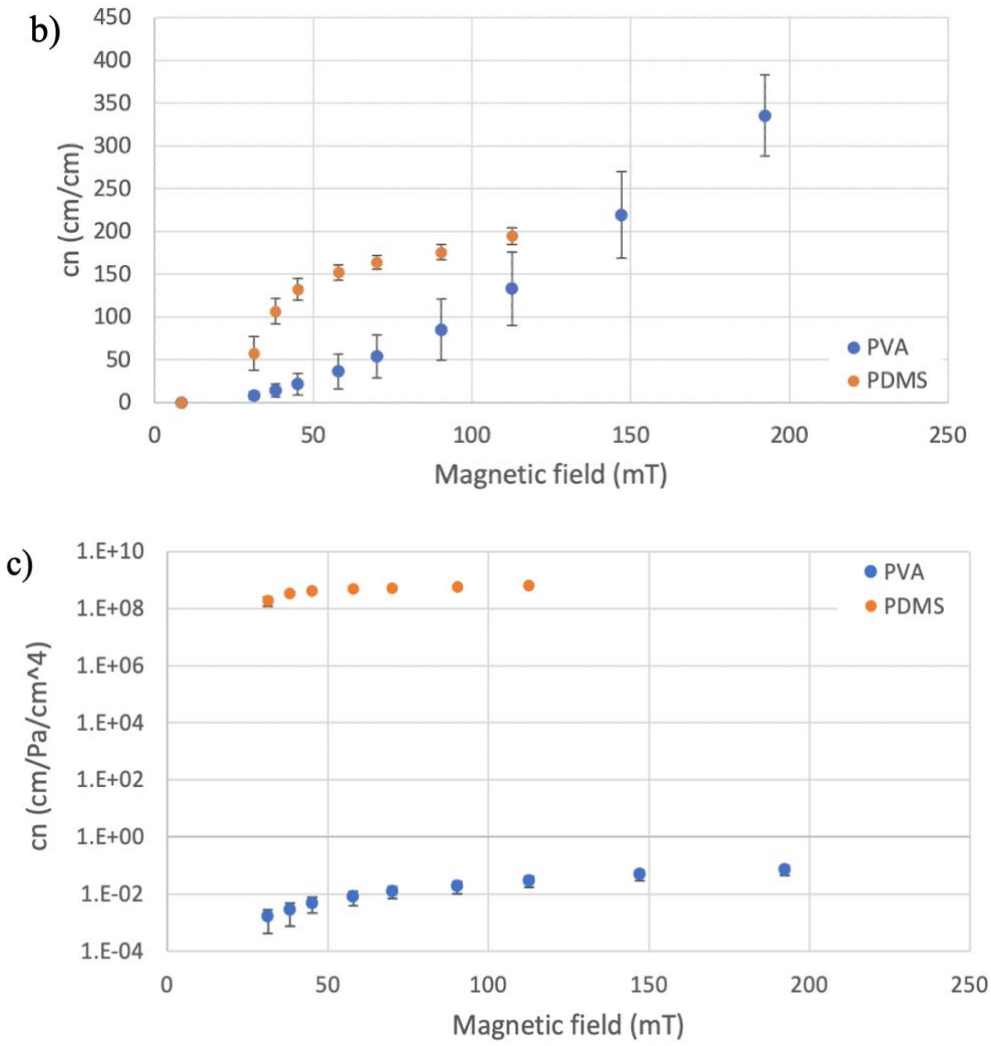

Figure 54. Displacement comparison of the bottom tips in the horizontal setup between iron oxide-PDMS and iron oxide-PVA samples (a) without normalization, and normalized by (b) thickness and (c) EI.

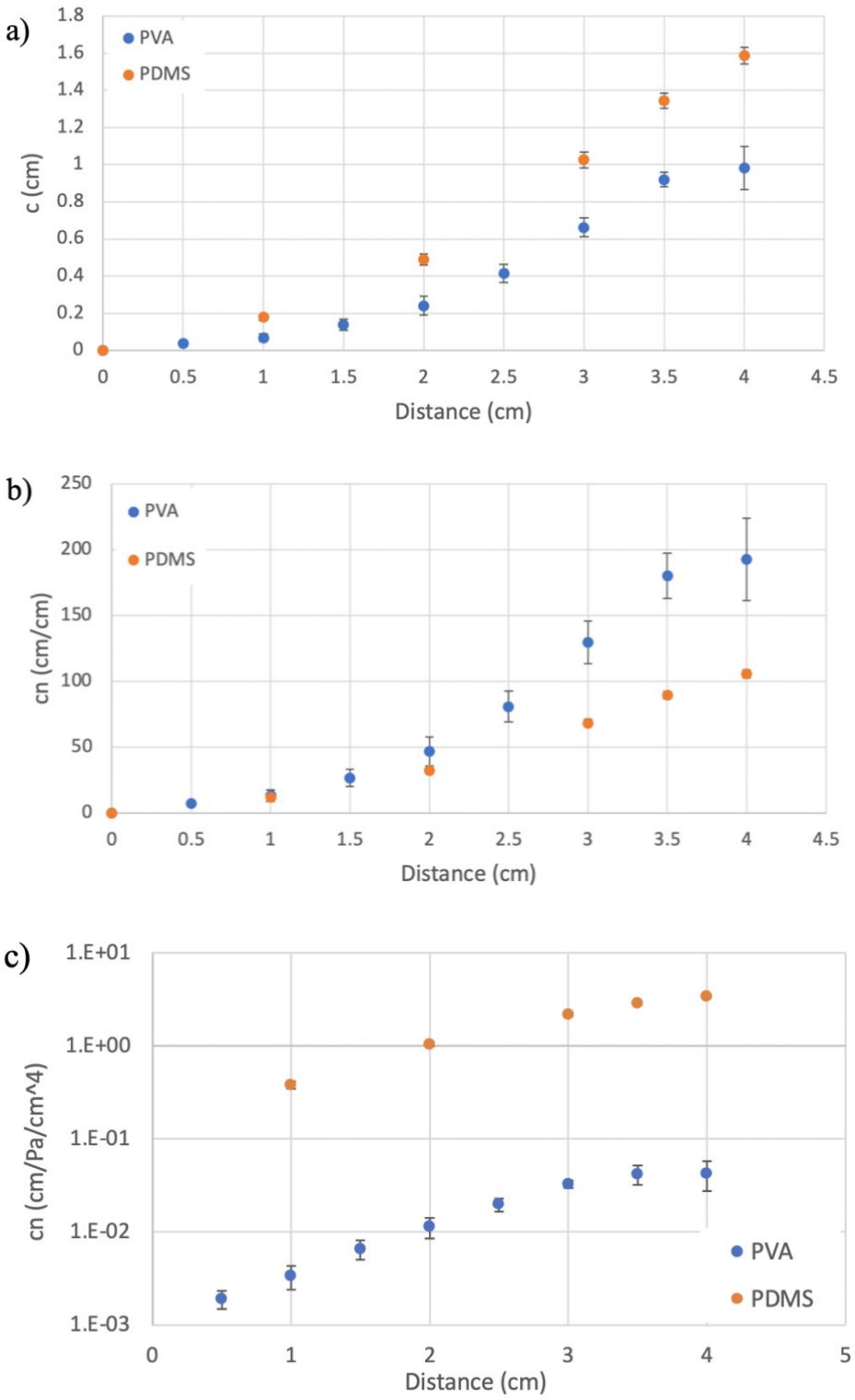

Figure 55. Displacement comparison of the bottom tips in the vertical setup between iron oxide-PDMS and iron oxide-PVA samples (a) without normalization, and normalized by (b) thickness and (c) EI.

4.2 Characterization comparison

Tensile test was also conducted on iron oxide-PVA thin films as shown in Figure 56. The Young's modulus is shown in the slope as 1895.2 MPa, which is much greater than that of MAEs shown in Figure 47. The Young's modulus indicated that PVA has a much greater stiffness which may affect the degree of actuation.

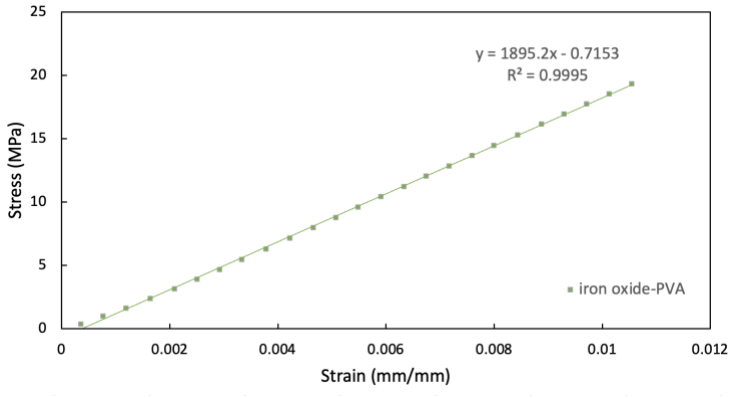

Figure 56. The stress-strain curve of iron oxide-PVA thin films.

Figure 57 illustrates the heat flow cycles for PVA pellets and a 10wt% PVA sample. The heat flows showed the T_g of PVA to be around 80°C. The first cycle indicated there were water inside the PVA that was not completely evaporated, which could affect the resulting mechanical properties.

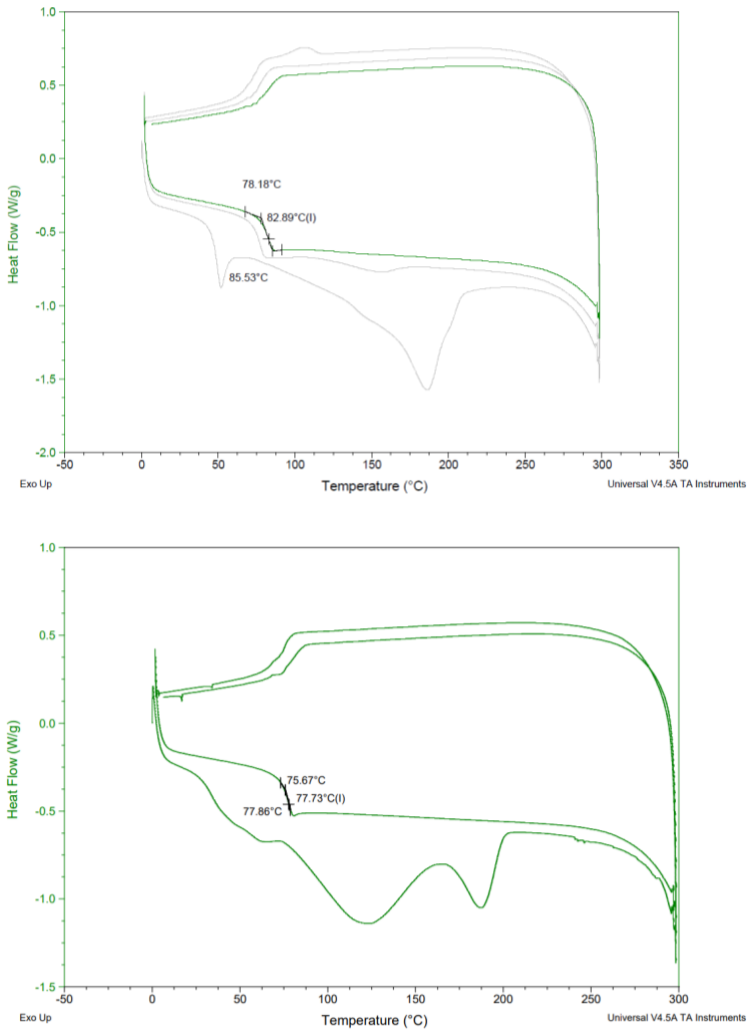

Figure 57. Cycles of DSC on PVA pellets (top) and PVA 10wt% sample (bottom).

DSC on iron oxide-PVA samples was conducted as well. As shown in Figure 58, a T_g of 80°C was also shown in the composite.

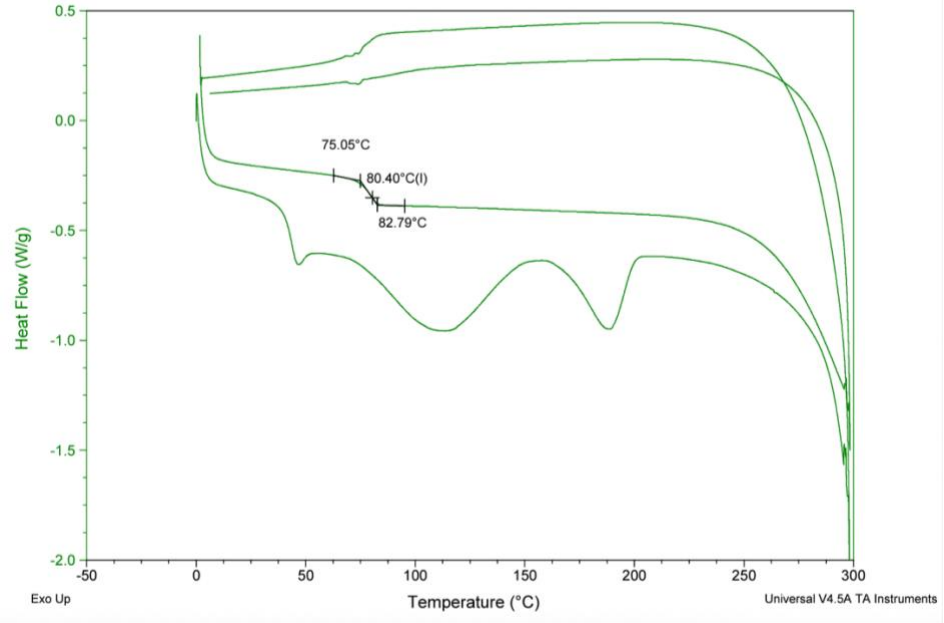

Figure 58. Cycles of DSC on iron oxide-PVA samples.

OM was performed to compare the patterns of dispersion in 30wt% iron oxide-PDMS and iron oxide-PVA thin films, as shown in Figure 59. The results show well dispersions of the particles in both matrices as no agglomeration was observed.

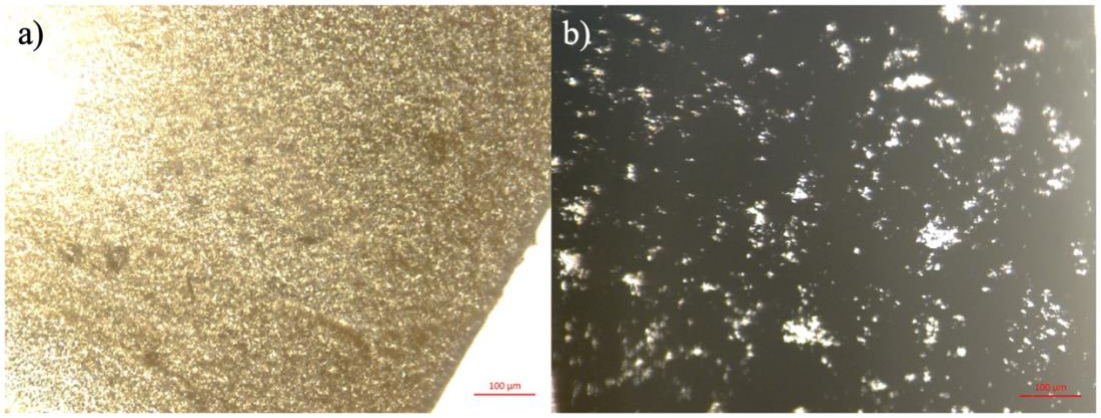

Figure 59. OM of 30wt% (a) iron oxide-PDMS and (b) iron oxide-PVA.

In addition, iron oxide-PVA composites with particle alignments was investigated. While the resulted composite failed to form a uniform thin film as iron oxide particles clustered together and changed the film structure under the magnetic field, interesting anisotropy of the particles were observed as shown in Figure 60.

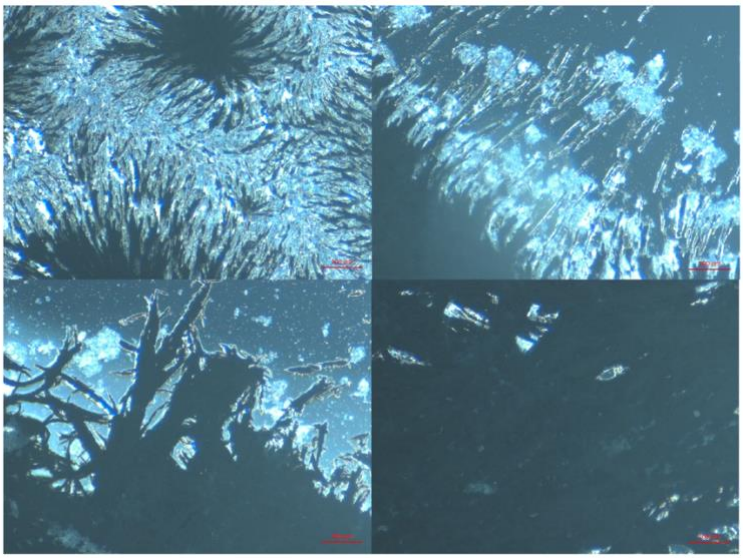

Figure 60. OM on aligned iron oxide-PVA composites

To further investigate the composite structures through the cross-section of the composites, scanning electron microscopy (SEM) was conducted on both 30wt% iron oxide-PDMS and iron oxide-PVA, as shown in Figure 61. The images show a well dispersed isotropy structure of the composites, while iron oxide-PVA looks denser with small degree of agglomeration, with both samples having the same thickness of 0.05 mm.

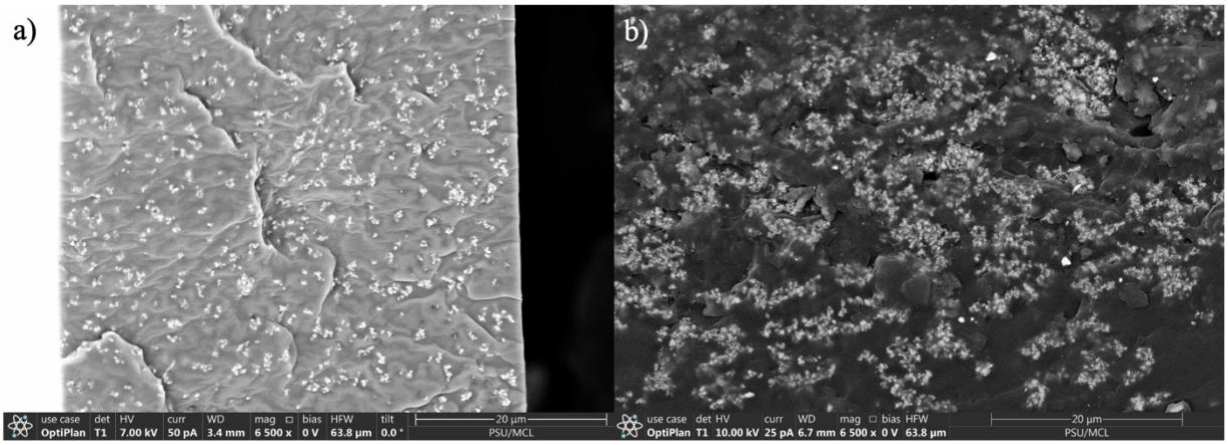

Figure 61. SEM on (a) 30wt% iron oxide-PDMS and (b) 30wt% iron oxide-PVA samples.

Chapter 5

Multi-field actuation using magnetic and thermal fields

5.1 Multi-field actuation with conventionally cast MAE-SMP

In order to demonstrate and investigate the degree of multi-field actuation, MAEs were combined with shape memory polymers (SMPs). Chapter 2 section 2.1.2 discussed the material composition and T_g of SMPs, and explained the shape memory cycle. SMPs were selected for their shape memory effect under changing temperatures and their material compositions were tuned using thickening agents, which was discussed in Chapter 2 section 2.2.2. In the first step, multi-field actuation was experimented using both conventionally-cast MAEs and SMPs under external magnetic and thermal field. Figure 62 demonstrated a full shape changing, locking and recovery cycle with control using both magnetic and thermal field. The external magnetic field was applied using a permanent magnet and the thermal field was applied using a hot water bath at 100°C, which was above the T_g of SMPs. The gripper was first submerged in the hot water bath while under applied magnetic field to prove multi-field actuation. The SMPs softened and allowed the MAEs on the tips of the fingers to react and deform towards the permanent magnet. After being taken out of the hot bath and slowing returning to room temperature, the gripper locked into the temporary position, which is the "gripping" state, without the presence of external magnetic field. To achieve shape recovery, the gripper was simply resubmerged into the hot water bath and showing the "releasing" state. However, the decrease in temperature of the hot water happened in a short period of time and thus using hot water to introduce the thermal field was not the most ideal heat source.

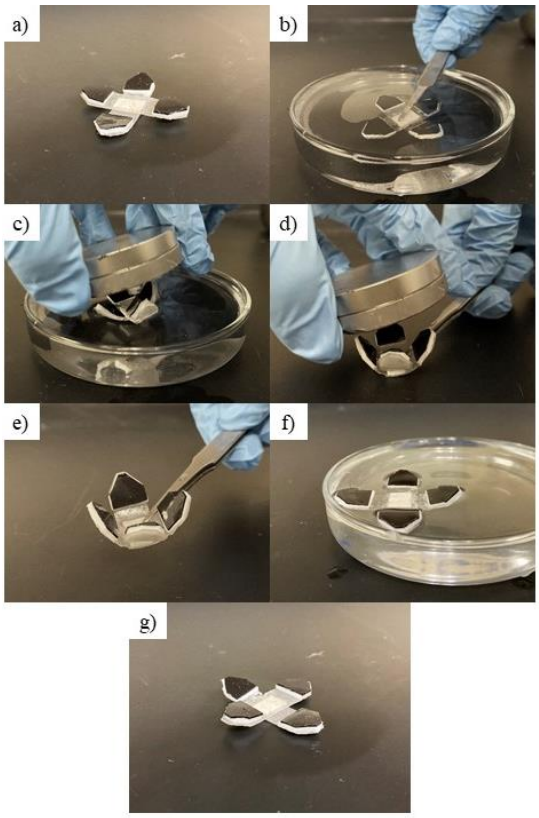

Figure 62. The shape programming and recovery process of the gripping actuation using combined MAE and SMP composites. A) The sample at its permanent position at room temperature. B) By soaking the sample in a hot water bath, the SMP became soft and easy to deform. C) An external magnetic field was applied to the MAE segments while the SMP strips were softened. D) The sample was moved to room temperature while holding the permanent magnet close to maintain the deformation. E) After 20 seconds under room temperature, the sample was locked into the temporary position by the stiffness of the SMP. F) The sample recovered its permanent position after resubmerging it in the hot water bath. G) The sample after shape change and recovery.

5.2 Multi-field actuation with printed iron oxide-SMP

After demonstrating feasibility of multi-field actuation, reactive extrusion additive manufacturing (REAM) was designed to print magneto-active polymer-based materials by passively mixing thermoset precursors and depositing them via a robotically positioned nozzle, after which the material was allowed to cure in situ [36]. This is accomplished at our collaborators' research group at University of Texas at Austin by Dr. Seepersad and Dr. Uitz. To simplify the material compositions for the printing design, SMPs were used as the polymer base and iron oxide microparticles were mixed inside the SMP matrix instead of PDMS elastomer. The system prepared two separate nozzles, one extruding pure SMP solution and the other extruding 30wt% iron oxide-SMP slurries. Figure 63 shows a printed thin film with thickness of 1 mm. The material composition changes as more iron oxide-SMP and less pure SMP were extruded and each two rasters represent a material composition change as marked. The film changed color to complete black even with the least amount of iron oxide being present, starting with 20% iron oxide-SMP.

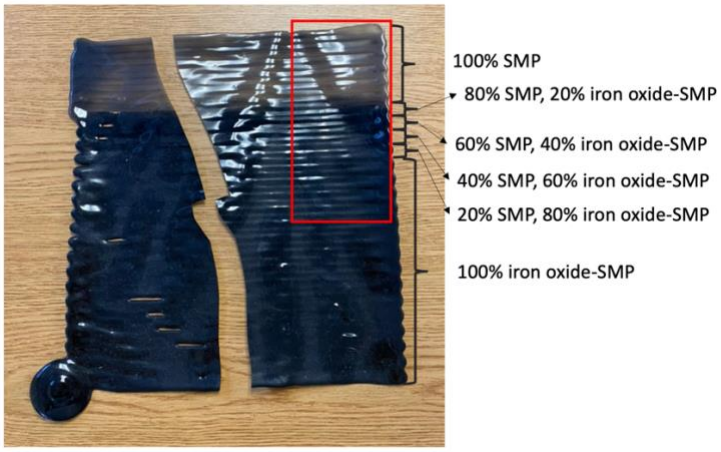

Figure 63. Printed MAE-SMP with various compositions as two different nozzles extruding 100% SMP and 30wt% iron oxide-SMP.

To investigate the effect of functional gradient on the actuation, four different 3.5×1 cm thin strips were cut out from the printed film, each obtaining a different composition of the iron oxide-SMP, as shown in Figure 64.

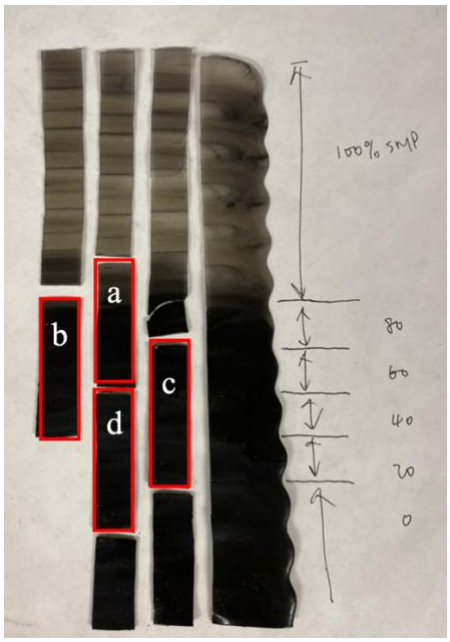

Figure 64. Samples a, b, c and d cut out from the printed thin film, each containing 3 different material compositions.

Table 11. Material composition details for each sample. Each composition takes up one-third of the sample.

Samples	Compositions
a	0% iron oxide-SMP, 100% SMP 20% iron oxide-SMP, 80% SMP 40% iron oxide-SMP, 80% SMP
b	20% iron oxide-SMP, 80% SMP 40% iron oxide-SMP, 60% SMP 60% iron oxide-SMP, 40% SMP
c	40% iron oxide-SMP, 60% SMP 60% iron oxide-SMP, 40% SMP 80% iron oxide-SMP, 20% SMP
d	60% iron oxide-SMP, 40% SMP 80% iron oxide-SMP, 20% SMP 100% iron oxide-SMP, 0% SMP

All four samples were tested for actuation using both external magnetic field and thermal field. The setup used is illustrated in Figure 65. A heat gun was applied at 15 cm away from the sample, constantly blowing hot air and maintaining the samples at 95°C. Particularly, sample b and d showed the most representative results as shown in Figure 66 and Figure 67. Figure 66a shows the actuation when 20% iron oxide-PDMS was at top and 60% iron oxide-PDMS was at bottom, and the sample was placed upside down in Figure 66b. Large difference in degree of actuation was observed in as the larger iron oxide percentage elicited a larger actuation at the bottom. Similar actuation difference was observed in Figure 67 as well. Figure 67a shows the actuation when 60% iron oxide-PDMS was at top and 100% iron oxide-PDMS was at bottom, and the sample was placed upside down in Figure 67b. However, the difference was much smaller than sample b, indicating larger amount of iron oxide achieves similar degree of actuation.

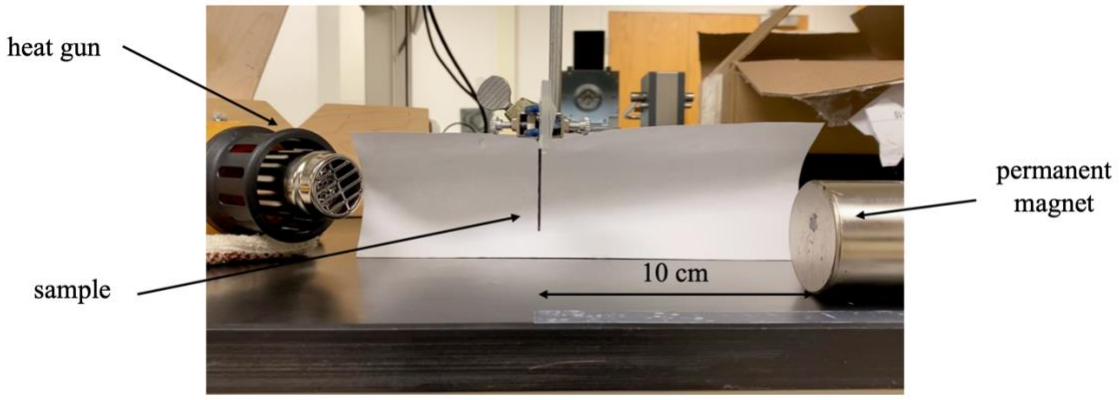

Figure 65. The setup for functional gradient actuation.

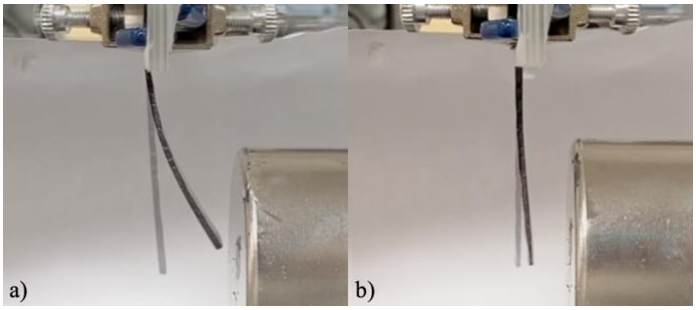

Figure 66. Sample b actuation comparison between (a) 20% iron oxide-PDMS at top and 60% iron oxide-PDMS at bottom, and (b) 60% iron oxide-PDMS at top and 20% iron oxide-PDMS at bottom.

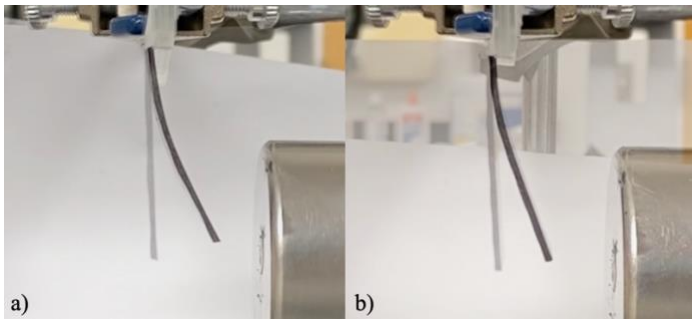

Figure 67. Sample d actuation comparison between (a) 60% iron oxide-PDMS at top and 100% iron oxide-PDMS at bottom, and (b) 100% iron oxide-PDMS at top and 60% iron oxide-PDMS at bottom.

Chapter 6

Conclusions

6.1 Significant findings

This study has proved that magneto-active polymer-based materials yield large actuation with both hard and soft magnetic particles under external magnetic field. Degree of bending was compared between PDMS matrix and PVA matrix, and the former shows a larger actuation than the latter due to higher elasticity to allow deformation.

Functional gradient introduces more complexity in material compositions and has effects on the degrees of actuation. The higher the weight percentage at the tip is, the larger the actuation is elicited. Functional gradient achieves multiple degrees of actuation from one single composite based on the placement of the sample, and thus allows more flexibilities in design complexity.

Printability for both MAEs and SMPs has been proved and the additive manufactured samples have shown large actuation results and potentials in more complex design for the proposed devices in the biomedical field.

6.2 Conclusions

This thesis investigated the actuation of magneto-active polymer-based materials using different polymer matrices, tested printability of MAEs and SMPs, and demonstrated the multi-field actuation using both conventionally-cast and printed MAEs and SMPs. The actuation was first demonstrated using MAEs with hard and soft magnetic particles. With hard magnetic particles, magnetic field was used to polarize the magnetic dipole directions of the particles and thus forming anisotropic structure inside the polymer matrix. Unimorph actuation of bending and

folding into a “V” and an “S” shape was demonstrated using BHF-PDMS with polarized particles into designed shapes under uniform magnetic field generated from an electromagnet. With soft magnetic particles, induced dipoles were elicited when external magnetic field was applied, and thus were actuated using permanent magnet. Bending and gripping motions were successfully observed from iron oxide-PDMS unimorph. Combinations of different materials or compositions were experimented as well. The gripper designed using BHF-PDMS and iron oxide-PDMS allowed different degrees of bending. The BHF-PDMS fingers clutched together when aligning with the magnetic field while iron oxide-PDMS fingers showed smaller degree of actuation by bending downward. Iron oxide-PDMS with 5wt% and 30wt% compositions yielded different response rates and degrees of actuation under magnetic field, which symbolized flower blooming motion as each petal blooms at different speeds. The results showed successful actuations and indicated more possibilities of complex actuation configurations with combinations of various materials. The printability using iron oxide-PDMS slurries was tested, and the addition of 5wt% of fumed silica yielded best performances from both printing and characterization results. Based on the printability tests, the feasibility of 3D printing MAEs and SMPs via REAM system was successfully demonstrated, which was tested and analyzed later in this study. In addition to PDMS, PVA was used as the matrix for magneto-active materials. As PVA is stiffer than PDMS, the mechanical properties of the matrix were expected to affect the actuation performance. After proving feasibility of actuating using external magnetic field, SMPs were studied for multi-field control. With the control of magnetic field and thermal field, non-contact large actuation of the unimorph structure using conventionally-cast MAEs and SMPs was achieved. A gripper designed was successfully actuated using both fields, demonstrating shape memory locking and recovery and magneto-active property. With printability of both MAE and

SMP slurries proved in the previous steps, REAM system was adapted to print iron oxide-SMP composites. The mechanical and magnetic properties of the printable samples were proved to be similar to those made by conventional casting from the tensile tests and characterization results. The printable samples successfully demonstrated contactless actuation and large ranges of deflection. Functional gradient was also demonstrated using both conventionally-cast and printed materials, showing a difference in degree of actuation with different material compositions. The conclusions of this thesis can be summarized in the following:

1. This study proved that MAEs yielded large actuation with both hard and soft magnetic particles using external magnetic field. Using PDMS elastomer as matrix with high elasticity allows large actuation in both bending and folding with designed unimorph structures.
2. Iron oxide-PDMS slurries are printable with the addition of fumed silica, with good interlayer adhesion and similar mechanical and magnetic properties to conventionally cast samples.
3. Normalizing the data by the thickness Young's modulus and moment of inertia led to significant changes between the actuation displacements of iron oxide-PDMS and iron oxide-PVA samples, which could be potentially due to significant difference in mechanical properties such as the Young's modulus of PDMS and PVA.
4. The results from this study indicated that additively manufactured magneto-active polymers combined with SMPs can result in actuation.

6.3 Future work

The next step is to use REAM system to additively manufacture more complex structures. By using REAM, successive layers of MAE and SMP can be deposited in preprogrammed locations to tune the local shape memory and magnetic response of additively manufactured

composite parts. Potential biomedical applications can be investigated and adapt 3D printed magneto-active polymers into structures.

Potential applications and devices in biomedical field can be explored in the next step as well. Some of the applications that are found promising are children's prosthetics that can grow with their bodies, braces that offer support for posture correction and restrict painful movement as each user's condition improves, and stents that can be customized for each user's unique anatomy.

References

[1] A. Gupta, A. Maharjan, and B. S. Kim, "Shape memory polyurethane and its composites for various applications," *Applied Sciences (Switzerland)*, vol. 9, no. 21, Nov. 01, 2019. doi: 10.3390/app9214694.

[2] T. Cheng *et al.*, "Bio-Inspired Motion Mechanisms: Computational Design and Material Programming of Self-Adjusting 4D-Printed Wearable Systems," *Advanced Science*, vol. 8, no. 13, Jul. 2021, doi: 10.1002/advs.202100411.

[3] C. Lin *et al.*, "4D-Printed Biodegradable and Remotely Controllable Shape Memory Occlusion Devices," *Advanced Functional Materials*, vol. 29, no. 51, Dec. 2019, doi: 10.1002/adfm.201906569.

[4] Y. Wong, J. Kong, L. K. Widjaja, and S. S. Venkatraman, "Biomedical applications of shape-memory polymers: How practically useful are they?," *Science China Chemistry*, vol. 57, no. 4. pp. 476–489, 2014. doi: 10.1007/s11426-013-5061-z.

[5] R. Pfeifer, C. W. Müller, C. Hurschler, S. Kaierle, V. Wesling, and H. Haferkamp, "Adaptable orthopedic shape memory implants," in *Procedia CIRP*, 2013, vol. 5, pp. 253–258. doi: 10.1016/j.procir.2013.01.050.

[6] M. Zarek, M. Layani, I. Cooperstein, E. Sachyani, D. Cohn, and S. Magdassi, "3D Printing of Shape Memory Polymers for Flexible Electronic Devices," *Advanced Materials*, vol. 28, no. 22, pp. 4449–4454, Jun. 2016, doi: 10.1002/adma.201503132.

[7] G. M. S. Paiva, L. G. T. A. Duarte, M. M. Faleiros, T. D. Z. Atvars, and M. I. Felisberti, "Photoactive polyurethanes based on 2,2′-dihydroxyazobenzene fluorescent segments," *Journal of Molecular Liquids*, vol. 337, Sep. 2021, doi: 10.1016/j.molliq.2021.116481.

[8] F. Pirmoradi, L. Cheng, and M. Chiao, “A magnetic poly(dimethylesiloxane) composite membrane incorporated with uniformly dispersed, coated iron oxide nanoparticles,” *Journal of Micromechanics and Microengineering*, vol. 20, no. 1, Jan. 2010, doi: 10.1088/0960-1317/20/1/015032.

[9] L. A. Makarova, Y. A. Alekhina, T. S. Rusakova, and N. S. Perov, “Tunable Properties of Magnetoactive Elastomers for Biomedical Applications,” in *Physics Procedia*, 2016, vol. 82, pp. 38–45. doi: 10.1016/j.phpro.2016.05.008.

[10] J. J. Martin, B. E. Fiore, and R. M. Erb, “Designing bioinspired composite reinforcement architectures via 3D magnetic printing,” *Nature Communications*, vol. 6, Oct. 2015, doi: 10.1038/ncomms9641.

[11] J. H. Koo, A. Dawson, and H. J. Jung, “Characterization of actuation properties of magnetorheological elastomers with embedded hard magnetic particles,” in *Journal of Intelligent Material Systems and Structures*, Jun. 2012, vol. 23, no. 9, pp. 1049–1054. doi: 10.1177/1045389X12439635.

[12] Y. Kim, H. Yuk, R. Zhao, S. A. Chester, and X. Zhao, “Printing ferromagnetic domains for untethered fast-transforming soft materials,” *Nature*, vol. 558, no. 7709, pp. 274–279, Jun. 2018, doi: 10.1038/s41586-018-0185-0.

[13] G. v. Stepanov, D. Y. Borin, Y. L. Raikher, P. v. Melenev, and N. S. Perov, “Motion of ferroparticles inside the polymeric matrix in magnetoactive elastomers,” *Journal of Physics Condensed Matter*, vol. 20, no. 20, May 2008, doi: 10.1088/0953-8984/20/20/204121.

[14] P. Zhu, W. Yang, R. Wang, S. Gao, B. Li, and Q. Li, "4D Printing of Complex Structures with a Fast Response Time to Magnetic Stimulus," *ACS Applied Materials and Interfaces*, vol. 10, no. 42, pp. 36435–36442, Oct. 2018, doi: 10.1021/acsami.8b12853.

[15] R. Bayaniahangar, S. Bayani Ahangar, Z. Zhang, B. P. Lee, and J. M. Pearce, "3-D printed soft magnetic helical coil actuators of iron oxide embedded polydimethylsiloxane," *Sensors and Actuators, B: Chemical*, vol. 326, Jan. 2021, doi: 10.1016/j.snb.2020.128781.

[16] Q. Ze *et al.*, "Magnetic Shape Memory Polymers with Integrated Multifunctional Shape Manipulation," *Advanced Materials*, vol. 32, no. 4, Jan. 2020, doi: 10.1002/adma.201906657.

[17] S. Qi, H. Guo, J. Fu, Y. Xie, M. Zhu, and M. Yu, "3D printed shape-programmable magneto-active soft matter for biomimetic applications," *Composites Science and Technology*, vol. 188, Mar. 2020, doi: 10.1016/j.compscitech.2019.107973.

[18] T. Kimura, Y. Umehara, and F. Kimura, "Fabrication of a short carbon fiber/gel composite that responds to a magnetic field," *Carbon*, vol. 48, no. 14, pp. 4015–4018, Nov. 2010, doi: 10.1016/j.carbon.2010.07.005.

[19] J. Cui *et al.*, "Nanomagnetic encoding of shape-morphing micromachines," *Nature*, vol. 575, no. 7781, pp. 164–168, Nov. 2019, doi: 10.1038/s41586-019-1713-2.

[20] Y. Lei, Z. Sheng, J. Zhang, J. Liu, W. Lv, and X. Hou, "Building Magnetoresponsive Composite Elastomers for Bionic Locomotion Applications," *Journal of Bionic Engineering*, vol. 17, no. 3, pp. 405–420, May 2020, doi: 10.1007/s42235-020-0033-4.

[21] Z. D. Xu, S. Suo, J. T. Zhu, and Y. Q. Guo, "Performance tests and modeling on high damping magnetorheological elastomers based on bromobutyl rubber," *Journal of*

Intelligent Material Systems and Structures, vol. 29, no. 6, pp. 1025–1037, Apr. 2018, doi: 10.1177/1045389X17730909.

[22] W. Zhang, X. L. Gong, W. Q. Jiang, and Y. C. Fan, "Investigation of the durability of anisotropic magnetorheological elastomers based on mixed rubber," *Smart Materials and Structures*, vol. 19, no. 8, p. 085008, Aug. 2010, doi: 10.1088/0964-1726/19/8/085008.

[23] S. Wu, C. M. Hamel, H. J. Qi, and R. Zhao, "Evolutionary algorithm guided voxel-encoding printing of functional hard-magnetic soft active materials," *arXiv*. arXiv, Jan. 30, 2020. doi: 10.1002/aisy.202000060.

[24] D. Sindersberger, A. Diermeier, N. Prem, and G. J. Monkman, "Printing of hybrid magneto active polymers with 6 degrees of freedom," *Materials Today Communications*, vol. 15, pp. 269–274, Jun. 2018, doi: 10.1016/j.mtcomm.2018.02.032.

[25] F. Zhang, L. Wang, Z. Zheng, Y. Liu, and J. Leng, "Magnetic programming of 4D printed shape memory composite structures," *Composites Part A: Applied Science and Manufacturing*, vol. 125, Oct. 2019, doi: 10.1016/j.compositesa.2019.105571.

[26] T. Kimura, Y. Umehara, and F. Kimura, "Magnetic field responsive silicone elastomer loaded with short steel wires having orientation distribution," *Soft Matter*, vol. 8, no. 23, pp. 6206–6209, 2012, doi: 10.1039/c2sm25442e.

[27] R. Tao *et al.*, "4D printed origami metamaterials with tunable compression twist behavior and stress-strain curves," *Composites Part B: Engineering*, vol. 201, Nov. 2020, doi: 10.1016/j.compositesb.2020.108344.

[28] T. Zhao, W. Dou, Z. Hu, W. Hou, Y. Sun, and J. an Lv, "Reconfigurable Soft Actuators with Multiple-Stimuli Responses," *Macromolecular Rapid Communications*, vol. 41, no. 17, Sep. 2020, doi: 10.1002/marc.202000313.

[29] A. Paolini, S. Kollmannsberger, and E. Rank, “Additive manufacturing in construction: A review on processes, applications, and digital planning methods,” *Additive Manufacturing*, vol. 30. Elsevier B.V., Dec. 01, 2019. doi: 10.1016/j.addma.2019.100894.

[30] O. Uitz, P. Koirala, M. Tehrani, and C. C. Seepersad, “Fast, low-energy additive manufacturing of isotropic parts via reactive extrusion,” *Additive Manufacturing*, vol. 41, May 2021, doi: 10.1016/j.addma.2021.101919.

[31] S. Bodkhe and P. Ermanni, “3D printing of multifunctional materials for sensing and actuation: Merging piezoelectricity with shape memory,” *European Polymer Journal*, vol. 132, Jun. 2020, doi: 10.1016/j.eurpolymj.2020.109738.

[32] M. A. al Masud, C. Breznak, P. von Lockette, and Z. Ounaies, “On the electric and magnetic alignment of magnetoactive barium hexaferrite-PDMS composites,” in *Behavior and Mechanics of Multifunctional Materials and Composites 2017*, Apr. 2017, vol. 10165, p. 1016513. doi: 10.1117/12.2263607.

[33] H. Tadokoro, S. Seki, and I. Nitta, “The Densities of Polyvinyl Alcohol Film at Moist States,” 1954.

[34] N. Jain, V. K. Singh, and S. Chauhan, “A review on mechanical and water absorption properties of polyvinyl alcohol based composites/films,” *Journal of the Mechanical Behavior of Materials*, vol. 26, no. 5–6. Walter de Gruyter GmbH, pp. 213–222, Dec. 20, 2017. doi: 10.1515/jmbm-2017-0027.

[35] I. D. Johnston, D. K. McCluskey, C. K. L. Tan, and M. C. Tracey, “Mechanical characterization of bulk Sylgard 184 for microfluidics and microengineering,” *Journal of Micromechanics and Microengineering*, vol. 24, no. 3, 2014, doi: 10.1088/0960-1317/24/3/035017.

[36] R. Leng, O. Uitz, Z. Ounaies, and C. Seepersad, “Design and characterization of a multilayered multifield-actuated polymer unimorph,” Proceedings of the American Society of Mechanical Engineers Conference on Smart Materials. 2021.